Astronomy & Astrophysics manuscript no. output
July 15, 2024

Mode identification and ensemble asteroseismology of 164 β Cep stars discovered from *Gaia* light curves and monitored by TESS

D. J. Fritzewski[1], M. Vanrespaille[1], C. Aerts[1,2,3], and D. Hey[4]

[1] Institute of Astronomy, KU Leuven, Celestijnenlaan 200D, 3001, Leuven, Belgium
e-mail: dario.fritzewski@kuleuven.be
[2] Department of Astrophysics, IMAPP, Radboud University Nijmegen, PO Box 9010, 6500 GL Nijmegen, The Netherlands
[3] Max Planck Institut für Astronomie, Königstuhl 17, 69117 Heidelberg, Germany
[4] Institute for Astronomy, University of Hawaii, 2680 Woodlawn Drive, Honolulu, HI 96822-1839, USA

ABSTRACT

Context. The *Gaia* mission discovered many new candidate β Cephei (β Cep) pulsators, whose variability classification is meanwhile confirmed from Transiting Exoplanet Survey Satellite (TESS) space photometry of the nominal mission.
Aims. We aim to analyse all currently available TESS data for these β Cep pulsators, of which 145 were new discoveries, in order to exploit their asteroseismic potential. β Cep stars belong to an under-represented class of pulsators in the current space photometry revolution while being of critical importance to improve evolution models of massive stars.
Methods. We extracted light curves for 216 star from the TESS full-frame images and performed pre-whitening to derive all significant frequencies. Based on *Gaia* Data Release 3, we deduced stellar properties and compared them to those of known β Cep stars from the literature. We developed a methodology to identify the dominant pulsation modes of the β Cep stars from *Gaia* and TESS amplitude ratios and from the detection of rotationally-split multiplets. We used grid modelling to gain insights into the population of β Cep stars.
Results. With the combination of TESS and *Gaia*, we successfully identified the mode degrees for 198 stars in our sample. We find the majority to have a dominant dipole non-radial mode ($l = 1$). Many non-radial modes show splittings in their TESS frequency spectra. This allowed us to assemble a large set of split multiplets in β Cep stars and to calculate their envelope rotation, spin parameter, and the level of differential envelope-to-surface rotation. For the latter, we find an upper limit of 4, with most stars rotating almost rigidly. We also provide the asymmetries of the multiplets, which range from -0.15 to 0.15 with the majority being positive. Based on grid modelling, we provide mass, convective core mass, and age distributions for 164 stars.
Conclusions. By combining *Gaia* DR3 and TESS, we enable asteroseismology of β Cep pulsators as a population. Our study prepares for future detailed modelling based on individual frequencies of identified modes leading towards a better understanding of these massive pulsators, as crucial probes of stellar evolution theory.

Key words. Asteroseismology – Stars: oscillations (including pulsations) – Stars: massive – Stars: interiors – Stars: evolution – Stars: rotation

1. Introduction

β Cephei (β Cep) stars are core-hydrogen burning massive stars ($8 \lesssim M/M_\odot \lesssim 25$) pulsating in lower-order pressure (p-) or gravity (g-) modes. Despite being known for more than a century (Frost 1906; Guthnick 1913) their mode excitation mechanism only got explained 30 years ago by Moskalik & Dziembowski (1992), Gautschy & Saio (1993), and Dziembowski & Pamiatnykh (1993). The pulsations are driven by the heat mechanism (also known as κ mechanism) active in the partial ionisation zone of iron-like elements in the outer envelope. However, while mode excitation in β Cep stars is roughly understood, it remains incomplete. Indeed, more modes are detected in data than predicted by theory as revealed in some of the prototypical class members (Pamyatnykh et al. 2004; Daszyńska-Daszkiewicz & Walczak 2010; Daszyńska-Daszkiewicz et al. 2013). Their data show g-modes while they are predicted to be stable (i.e. non-pulsating). Moravveji (2016) provided a summary of observed modes in β Cep stars and illustrated the impact of higher opacities in the driving zone. Additional physical mechanisms may also be active in the interiors of such stars, while being absent in our current excitation theory. Microscopic atomic diffusion, notably radiative levitation, was recently shown to be one such missing mechanism (Rehm et al. 2024).

In addition to shortcomings on mode excitation, the identification of the geometrical configuration of the observed modes in β Cep stars remains poor. The geometry of the low-order modes of the β Cep stars is well described by a spherical harmonic, characterised by (l, m) representing the mode degree and azimuthal order. Identification of (l, m) is a prerequisite for asteroseismic modelling (Salmon et al. 2022). Our current work aims to improve this aspect of mode identification for this class of massive pulsators, by relying on space photometry. Before diving into this topic, it is useful to recall the history and basic properties of β Cep star pulsations.

The interest in β Cep stars came in waves of discoveries. The earliest work focused on the period determination from radial velocity time series of the very few known stars similar to β Cep and the lack of understanding of the instability mechanism (e.g. review by Struve 1952). In the following years, more β Cep stars were discovered and the efforts to understand the pulsation mechanism were continued, although the physical origin was still elusive (Lesh & Aizenman 1978). The discovery and explanation of the mode excitation mechanism (Pamyat-

nykh 1999, for a summary) sparked new interest in β Cep stars. Aerts et al. (1992, 1994) conducted successful mode identification from time series spectroscopy for a few bright class members, while Heynderickx et al. (1994) identified the degree of the dominant pulsation modes for a substantial number of class members from multi-colour photometry. While both methods worked, only a limited number of modes per star could be identified – often just one or two.

Based on the numerous discovered β Cep stars, Stankov & Handler (2005) composed a catalogue containing 93 genuine and 77 candidate β Cep stars. Yet, the majority of them lack a solid identification of their pulsation modes. The β Cep stars discovered from large ground-based surveys (e.g. Pigulski & Pojmański 2008; Labadie-Bartz et al. 2020) or dedicated observations of a few selected young open clusters (Saesen et al. 2013; Moździerski et al. 2019) suffer from the same limitation in terms of seismic probing power: too few or no pulsation modes have been identified.

Inferences of a β Cep star interior were achieved thanks to the 21 year-long photometric monitoring of HD 129929 (Aerts et al. 2003, 2004b; Dupret et al. 2004). These three dedicated studies kick-started β Cep asteroseismology from the identification of six modes: a radial mode, a rotationally split p-mode triplet and two components of a g-mode quintuplet. It led to the first seismic probing of the internal rotation of a main-sequence star other than the Sun, with the bottom of the envelope rotating about 4 times faster than the outer envelope. Inspired by this result, in coordinated efforts months-long multi-site campaigns involving tens of astronomers worldwide were organised. As such, four of the brightest β Cep stars got scrutinised seismically from combined multi-colour photometric and spectroscopic time-series data. These stars are still the best modelled β Cep stars today, thanks to the unambiguous identification of their modes: ν Eri (Aerts et al. 2004a; De Ridder et al. 2004; Pamyatnykh et al. 2004), θ Oph (Handler et al. 2005; Briquet et al. 2005, 2007), 12 Lac (Handler et al. 2006; Dziembowski & Pamyatnykh 2008; Desmet et al. 2009), and V2052 Oph (Handler et al. 2012; Briquet et al. 2012). The seismic estimates of the internal rotation, age (in terms of core hydrogen mass fraction), and core boundary mixing are summarised in Bowman (2020).

With the new era of space photometry, asteroseismology has gained a treasure trove of high-quality, high-cadence data for many pulsating stars (Aerts 2021; Kurtz 2022, for recent reviews). For β Cep stars in particular, the earliest space-based observations with the Microvariability and Oscillations of Stars (MOST) satellite revealed multi-periodic behaviour of δ Ceti, which was thought to be a mono-periodic radial pulsator until that time (Aerts et al. 2006). The CoRoT mission advanced our knowledge of only three more β Cep stars (Belkacem et al. 2009; Degroote et al. 2009; Briquet et al. 2011; Aerts et al. 2019) and the *Kepler* space satellite did not reveal any additional β Cep pulsators with identified modes (Balona et al. 2011; Lehmann et al. 2011). This led to a paucity of research on these stars with space-based time series photometry, although asteroseismology as a whole was revolutionised by the *Kepler* mission.

Already with the first two sectors of the Transiting Exoplanet Survey Satellite (TESS, Ricker et al. 2015) mission it became obvious that massive star asteroseismology entered a new era (Pedersen et al. 2019). Shi et al. (2024) provide a catalogue of all β Cep stars observed by TESS with 2 min-cadence data. Southworth & Bowman (2022) identified eight β Cep pulsators in eclipsing binaries, while Eze & Handler (2024) recently expanded this list to 78 systems. However, to best study these stars long-baseline time series observations are needed to resolve the anticipated close-by frequencies and identify the pulsation modes.

Burssens et al. (2023) analysed the 352 d-long light curve of the bright HD 192575 located in the TESS Northern continuous viewing zone and were able to model its structure parameters with high precision as the fifth β Cep star with tight seismic constraints. They also estimated its internal rotation profile from forward modelling but encountered large uncertainty due to the use of only three rotationally split multiplets. Vanlaer et al. (in prep.) meanwhile analysed the 5-year TESS light curve (with twice a gap of about a year) and resolved some of the ambiguity in the mode identification, allowing the authors to perform rotation inversion.

Next to CoRoT, *Kepler*, and TESS, the *Gaia* mission has proven to be a highly successful gateway to discover pulsating stars. Despite not being designed for asteroseismology, the recurring visits to millions of stars in a quasi-random pattern allowed for the discovery of some 100,000 new main-sequence pulsators (Gaia Collaboration et al. 2023). Hey & Aerts (2024) revisited these stars and analysed their first two years of TESS photometry, confirming the main pulsation frequency and classification for more than 80% of these *Gaia*-identified pulsators. Given these findings, we are encouraged to focus on the 222 β Cep stars in the sample of Gaia Collaboration et al. (2023) and to follow up on the work of Hey & Aerts (2024) by considering the available TESS data.

Here, we use TESS light curves with a considerably longer time base than Hey & Aerts (2024), enabling as such maximal frequency resolution. Our aim is to hunt for resolved low-order pressure and gravity modes and rotational splitting in the 222 *Gaia*-discovered β Cep stars, opening pathways to mode identification and seismic modelling from combined TESS photometry and *Gaia* data, in a homogeneous way for an as large as possible ensemble of β Cep stars with publicly available light curves assembled with both satellites.

2. Data reduction

We selected all 222 variable stars classified by Gaia Collaboration et al. (2023) as β Cep stars as our initial sample. Since our work focuses on the synergy between the TESS and *Gaia* DR3 light curves, we only included these stars. Yet, we emphasise that the methods developed in this work could potentially be applied to TESS observations of known β Cep stars with *Gaia* time series photometry. To prepare for the data reduction, we obtained for each star on our target list its position from the *Gaia* archive and cross-matched it with the TESS input catalogue (Stassun et al. 2019; Paegert et al. 2021) to obtain its TIC ID.

2.1. TESS data reduction and light curve detrending

We employed the TESS data reduction pipeline `tessutils` (Garcia et al. 2022) which enables the end-to-end creation of detrended light curves from TESS full-frame images (FFI) and is optimised for the asteroseismic analysis. We briefly recall its work-flow here. For every TIC number, `tessutils` downloads cut-outs from the FIIs using `tesscut` (Brasseur et al. 2019). In the present work we chose a cut-out size of 25 px by 25 px. Subsequently, `tessutils` searches for the optimal aperture for each sector while trying to keep the contamination from neighbouring stars below 1 %. Afterwards, it extracts the light curve with the chosen aperture.

Since many of our stars are located in crowded fields near the Galactic plane or in open clusters, we weakened the contam-

ination criterion for stars with a large number of nearby sources. The targeted β Cep stars are typically among the brightest stars in the field they provide the main flux contribution. To reduce the influence of neighbouring stars, we set the aperture to a single pixel centred on the target's position. With this approach, we were able to obtain light curves for 37 stars that would otherwise have (partially) been missed.

After aperture photometry, `tessutils` detrends the extracted light curves with a principal component analysis per sector to remove long-term trends in the data. This is justified for the asteroseismic analysis of β Cep stars as we are interested in variability with periodicities of typically several hours for the individual modes. The normalised light curves were binned to the longest cadence of the TESS photometry, that is 30 min. This guarantees a homogeneous treatment involving all TESS FFI data of the sample stars discovered from *Gaia*, while it leads to excellent agreement among the dominant frequencies detected in the TESS and *Gaia* DR3 light curves, as we will show below. We tested that relying on the higher-cadence TESS FFI data does not change the results for our β Cep population study. Finally, the data of all sectors were stitched to a single long-term light curve per star.

Despite the initial detrending of the light curves, we still noticed significant instrumental trends in many light curves. Therefore, we manually selected and removed parts of the light curve where instrumental effects were dominant. Therefore, manually selected intervals of low-quality data were dismissed. To remove the remaining non-astrophysical trends, we fitted and subtracted a second order polynomial to sections of the light curve separated by a gap in the data of at least three hours. In some cases, we manually selected the section to ensure a smooth detrending. Afterwards, we σ-clipped each section with a threshold of $5\,\sigma$. Finally, in a handful of exceptional cases, an entire TESS sector was removed from the light curve due to excessive background flux or noise.

Out of our initial sample of 222 stars, 216 have been observed by TESS and we were able to obtain time series photometry for all of them. The number of sectors in the light curves range from one to seven with a median of four visits by TESS over the current mission lifetime spanning about five years.

2.2. Frequency extraction from pre-whitening

The method of pre-whitening consists in identifying the dominant signal frequency in the Fourier transform of the light curve, finding the amplitude and phase of that peak frequency and subtracting the matching sinusoid from the light curve to construct a residual light curve. Subsequently, the next strongest frequency is identified in the residuals, a sinusoid is built, and subtracted, etc. This procedure is followed until a user-specified stop criterion is reached (see, e.g. Chapter 5 in Aerts et al. 2010, for details).

In the case of our sample of 216 β Cep stars, each TESS light curve has its own complicated window function resulting from the month-long sectors of the TESS observations and the long gaps in between them. In order to extract all significant frequencies, we used a customised version of the pre-whitening module of the publicly available frequency analysis code `STAR SHADOW` (IJspeert et al. 2024). While the reader is referred to that paper for details on the methodology, we point out that `STAR SHADOW`'s pre-whitening procedure is computationally efficient compared to other pre-whitening routines (such as the five versions in Van Beeck et al. 2021) because it does not rely on time-consuming non-linear regression for all extracted signals simultaneously. Rather, it only resorts to non-linear regression for those signals that strongly affect each other. On top of that, `STAR SHADOW` is well suited to analyse blended frequency peaks in Fourier spectra, which are quite common in our set of light curves due to the limited coverage of the baseline.

During the frequency extraction via pre-whitening, `STAR SHADOW` relies on the Bayesian Information criterion (BIC) as its stopping criterion (Schwarz 1978). In order to avoid over-extraction of frequencies from the high-quality space photometry, we adopted ΔBIC>10 as criterion in each pre-whitening step. This means that a new frequency is only accepted as present in the data at a particular stage of pre-whitening if the BIC of its residual curve is reduced by at least a value of 10 compared to the BIC of the light curve in the previous stage of the pre-whitening. This is more conservative than the standard cutoff value of 2 adopted in many statistical applications (Kass & Raftery 1995).

We employed a hybrid method for the selection of the next signal to be pre-whitened. Herein, the pre-whitening initially uses the concept of amplitude hinting (e.g. Van Beeck et al. 2021) and swaps to signal-to-noise ratio (SNR) hinting if a frequency is initially rejected, where the noise level is computed over a range of $1\,\mathrm{d}^{-1}$ in the Fourier spectrum. If that or another potential signal is rejected again, the pre-whitening is terminated. For the final significance assessment of each signal at the end of the frequency extraction by `STAR SHADOW`, we increased the SNR-threshold by 0.25 as recommended by Baran & Koen (2021) for space photometric light curves with long gaps.

2.3. Extracted frequencies

We found between four and 36 (median 13) independent signals in each of our TESS light curves. These values already show that β Cep stars pulsate with few modes. It also reveals that our detrending removed most of the instrumental effects, that would contaminate the Fourier domain and lead to more extracted yet spurious frequencies.

To analyse a large number of pulsators, stacking and sorting the periodograms can reveal hidden structures (e.g. Li et al. 2020b; Hey & Aerts 2024). Figure 1 shows the extracted significant frequencies from the TESS photometry for our *Gaia*-observed sample sorted by the frequency of highest amplitude. Since β Cep stars show typically few excited low-order modes that do not occur in an asymptotic regime of high or low frequencies, no obvious structure emerges from this diagram. Nevertheless, this visual representation of the sample shows the range of detected significant frequencies. Further, it becomes obvious from the figure that the observed significant frequencies for a given star depend on the position of its dominant frequency.

2.4. Comparison to Gaia frequencies

Figure 2 compares the main frequency from our TESS analysis with the frequencies derived from *Gaia* DR3 by Gaia Collaboration et al. (2023). As already found by Hey & Aerts (2024), most of the pulsation frequencies agree very well, highlighting once again the potential of the *Gaia* time series photometry to discover non-radial pulsators at a level of 4 mmag or above. For stars without a matching primary frequency, we searched through other signals in order of decreasing amplitudes in the TESS data and matched them to the *Gaia* frequency. Once a

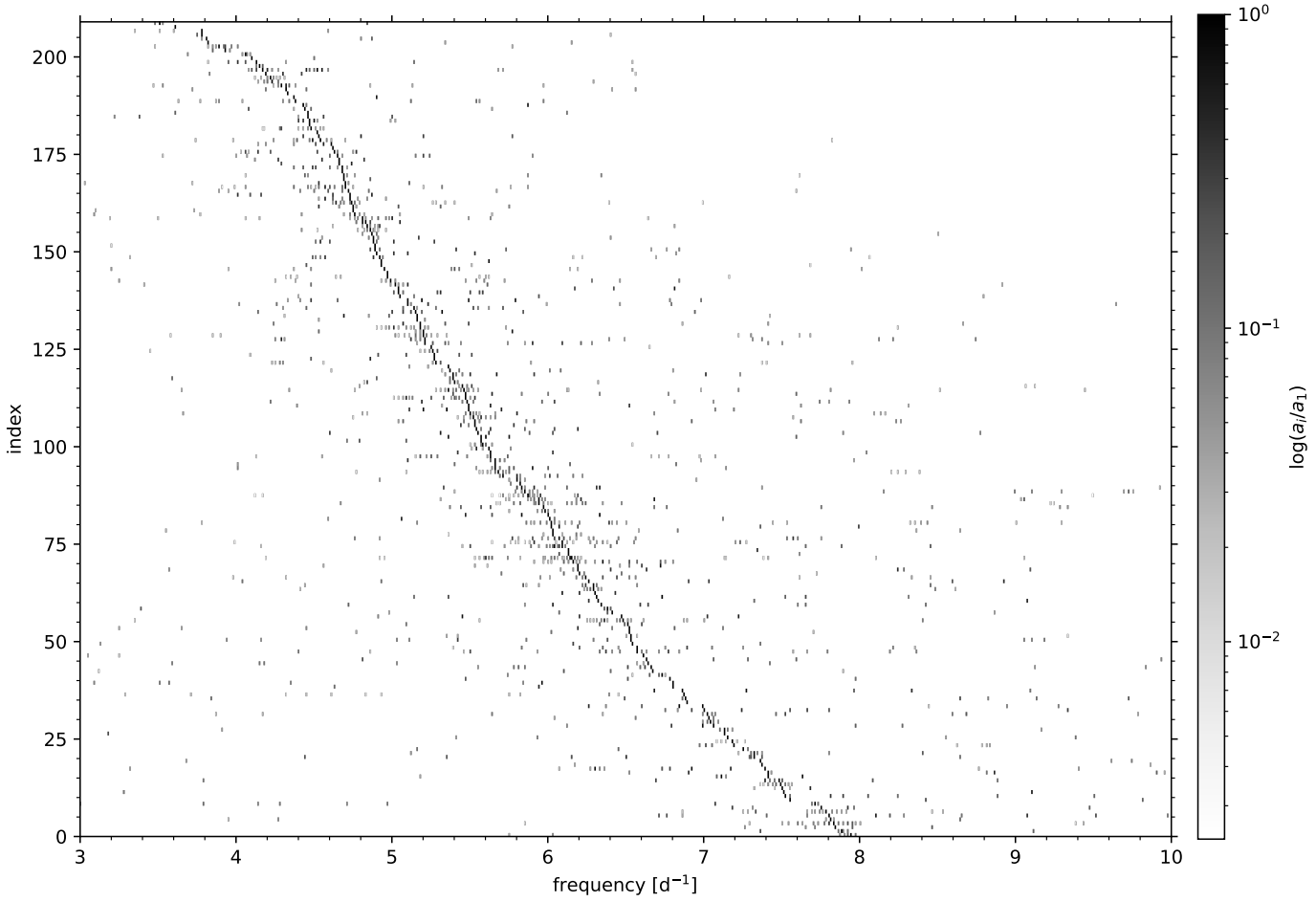

Fig. 1. Stacked representation of the extracted independent, significant frequencies for 212 of the *Gaia* discovered β Cep stars, sorted by the frequency with the largest amplitude. Most of the stars exhibit multi-periodic behaviour with excited modes over a large frequency range. The grey-scale gives the amplitudes relative to the largest amplitude of each star on a logarithmic scale. This figure includes only the stars whose main frequency occurs in the plotted β Cep range. Some stars have lower main frequencies and turn out to be SPB stars or β Cep/SPB hybrid pulsators with dominant high-order g-modes, or are dominated by other variability than pulsations.

match was found we stopped the search. For seven stars[1], we found no matching signal in the TESS data within our matching criterion $\Delta f < 0.006\,\mathrm{d}^{-1}$. The median difference between the TESS and *Gaia* matched frequencies is $\Delta\tilde{f} = 0.0013\,\mathrm{d}^{-1}$.

We limited the current analysis to the primary frequency detected with *Gaia*. Although we possess measurements of the secondary frequency from the *Gaia* DR3 time series photometry, we noticed that these frequencies match our extracted frequencies only for a minority of cases. Often, we find $f_{Gaia} > 10\,\mathrm{d}^{-1}$, whereas we rarely extracted any significant frequency in this range from TESS. It was already discussed by Gaia Collaboration et al. (2023) that the *Gaia* DR3 data suffer from instrumental effects at mmag level for the secondary frequencies, which may be connected to multiples of the satellite frequency of $4\,\mathrm{d}^{-1}$ for some of the variables. Hence for the β Cep population study in our work, using the secondary frequency from *Gaia* is not informative. We note that detailed work on certain stars might be able to derive additional constraints for the pulsation mode of the secondary frequency. Further, longer time series data as delivered by future *Gaia* data releases might provide more robust secondary frequencies in agreement with TESS.

[1] The seventh star is not shown in Fig. 2 because its *Gaia* frequency $f_{Gaia} = 21\,\mathrm{d}^{-1}$ is outside the β Cep frequency range. Yet this star might still be a β Cep pulsator as the dominant TESS frequency $f_1 = 6.6\,\mathrm{d}^{-1}$.

3. Stellar properties

3.1. Gaia *derived properties*

We aim to analyse the β Cep stars in our sample in a homogeneous way and hence chose to use stellar parameters from *Gaia* DR3. Of particular interest are the effective temperature ($T_{\rm eff}$) and the luminosity ($\log L/L_\odot$). Shi et al. (2023) show that the *Gaia* $T_{\rm eff}$ derived by the Extended Stellar Parametrizer for Hot Stars (ESP-HS, Fouesneau et al. 2023) is reliable for pulsating hot main sequence stars. We follow their example and use these values as the basis for our analysis.

In addition to the effective temperatures, we extracted positions, parallaxes, and G band fluxes for every target. Where available, we also added stellar parameters from ESP-HS and the General Stellar Parametrizer from Photometry (GSPPHOT). Unfortunately, the *Gaia* ESP-HS parameters are not available for all stars in our sample but only for 190 of the 222 stars. Hence, we are not able to place all the observed stars in the Hertzsprung-Russel diagrams (HRD).

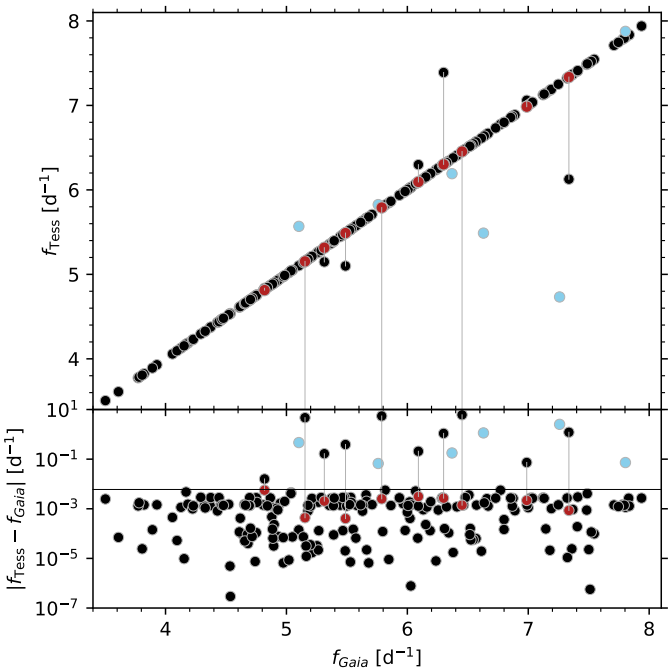

Fig. 2. Comparison between the *Gaia* and TESS frequencies for 215 stars. Top: TESS frequency $f_{\rm TESS}$ against the *Gaia* derived frequency f_{Gaia}. Black symbols indicate stars for which we found a match in frequency, red symbols show stars with matching frequencies for other than the dominant signal, and blue symbols indicate stars without a counterpart signal in the TESS data. Lines are connecting the offset frequencies to their matched counter part. For three stars the main frequency is below the plotting range. Bottom: Difference between the *Gaia* and TESS frequencies. The black line indicates our chosen threshold for matching signals ($\Delta f < 0.006\,\mathrm{d}^{-1}$).

To derive the stellar luminosity, we require a bolometric correction. The *Gaia* bolometric correction (Creevey et al. 2023) is only valid up to 10 000 K and β Cep stars are hotter with $15\,000\,K \leq T_{\rm eff} \leq 25\,000\,K$. Pedersen et al. (2020) derived bolometric correction functions for massive stars including the range of β Cep stars. We used these and calculated the luminosities $\log L/L_\odot$ based on the *Gaia* DR3 absolute magnitudes taking into account the reddening based on the ESP-HS estimate and the distance as determined by the GSPPHOT pipeline for OB stars, the general GSPPHOT values, or the inverse of the parallax depending on the availability.

The uncertainties of the parameters in the astrophysical parameters table are often underestimated (Fouesneau et al. 2023). In particular the effective temperature has an uncertainty much larger than the typically given 500 K ($\sim 2\,\%$). For the purpose of this work, we assumed an uncertainty of 10 % ($\Delta \log T_{\rm eff} = 0.043$ dex) for all stars in the sample, which is a reasonable estimate given the comparison in Fig. 15 of Fouesneau et al. (2023). The uncertainty of the luminosity is strongly dependent on the effective temperature through its use in the bolometric correction.

The *Gaia* ESP-HS parameters also include the projected surface rotational velocity $v \sin i$ calculated from the line broadening of the RVS spectra under the assumption that rotation determines the line broadening, which is a valid assumption (cf., Aerts et al. 2023). Together with the luminosity and effective temperature, which gives an estimate of the stellar radius, we can calculate the surface rotation rate of the stars. This parameter, $f_{\rm rot} \sin i$, is available for 167 stars. Although, it is not very precise with a typical uncertainty $\sim 40\,\%$, it will still be useful in our subsequent analysis.

3.2. Gaia *data of known* β *Cep stars*

To compare the properties of the *Gaia* discovered β Cep stars with these of known β Cep stars, we extracted their *Gaia* DR3 data as well. As the literature sample, we use the certain β Cep stars from the catalogues of Stankov & Handler (2005), Pigulski & Pojmański (2008), Labadie-Bartz et al. (2020), Shi et al. (2024), and Eze & Handler (2024). For each of the catalogues, we derived the same *Gaia* properties as described above. From the four catalogues in the literature, we find 582 stars of which 408 are classified as genuine β Cep stars. Among the 222 stars in the *Gaia*-discovered sample, 145 are not listed in any of the literature catalogues, bringing the total number of β Cep stars in the combined sample to 553 stars.

4. Population of β Cep stars

Before analysing our *Gaia* discovered sample in detail, we present the overall properties of the ensemble. Figure 3 shows all 442 stars (out of 553) with adequate *Gaia* ESP-HS parameters in an HRD. Most of the stars in our sample fall inside the instability strips for B-type pulsators calculated by Burssens et al. (2020). These are based on one particular choice of input physics so we expect some stars to occur outside that region as also stressed by Aerts & Tkachenko (2024), Rehm et al. (2024), and Hey & Aerts (2024).

Several stars from the literature occur in the colder slowly pulsating B star (SPB) instability region. We suspect that these stars were misclassified as β Cep stars in the literature but are rather SPB stars. All the new *Gaia*-derived β Cep stars fall inside or close to the β Cep instability strip and can hence from their HRD position and TESS variability characterisation (see below) safely be assumed to be genuine β Cep stars.

At $\log T_{\rm eff} \approx 4.5$, we find a gap between the bulk of the β Cep stars and a smaller group mostly containing stars from our new sample. With only the *Gaia* ESP-HS data, we cannot be certain whether this gap is astrophysical or introduced by the intricate parameter estimation procedure. It is present in the entire ESP-HS data set. We note the position of the gap overlaps with the transition from spectral type O to B (Pecaut & Mamajek 2013). In case the gap is physical these stars on the hotter side of the blue border of the strip would be of great interest for follow-up observations and detailed asteroseismic modelling as these stars might be binary or merger products (Fabry et al. 2022, 2023; Bellinger et al. 2024; Henneco et al. 2024).

4.1. *Detailed analysis of the* Gaia *sample*

After verifying that all of our sample stars with *Gaia* ESP-HS parameters fall indeed into the parameter range of β Cep stars, we analyse their TESS light curves in more detail. In a visual inspection, three different light curve shapes emerge as the main sub-classes (Fig. 4). The first class comprises of mono-periodic light curves which show one dominant coherent oscillation over a TESS sector. On closer inspection after pre-whitening, these stars pulsate often in multiple frequencies as well but their secondary frequencies have small amplitudes compared to the dominant mode. Clearly multi-periodic pulsators constitute the second class. Their light curves exhibit modulations due to mode beating with periods between one and tens of days, as was al-

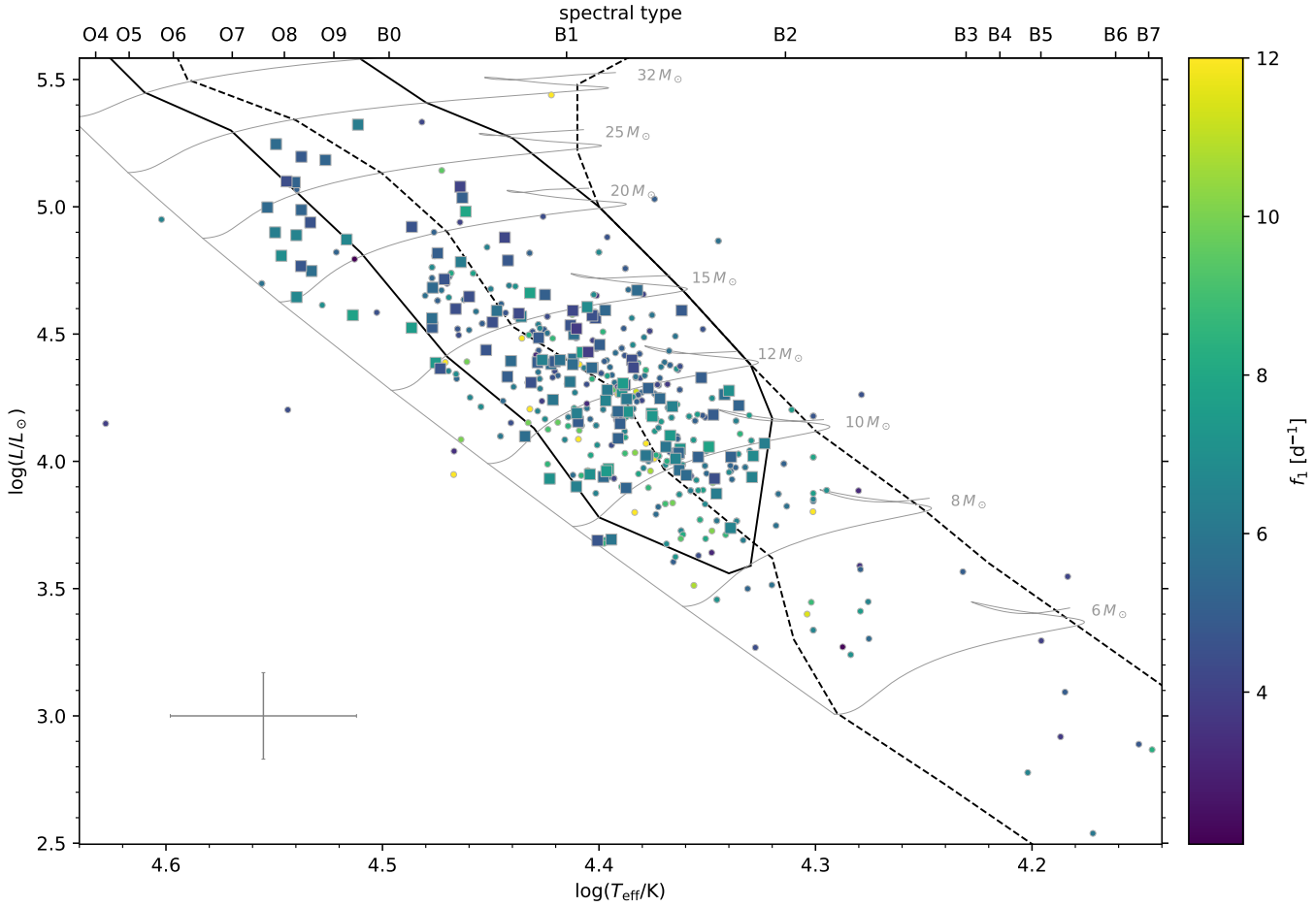

Fig. 3. Hertzsprung-Russel diagram based on *Gaia* data of all 321 β Cep stars from the literature (circles) and 121 new stars of our *Gaia*-informed sample (squares, new detections). The typical uncertainty is indicated in the lower left. As black outlines, we show the instability regions for p-modes (solid, β Cep), and g-modes (dashed, SPB) based on the calculations from Burssens et al. (2020). In the background, we added in grey main sequence evolutionary tracks from Burssens et al. (2020). The colour-code gives the main pulsation frequency of the stars cut-off at 12 d^{-1}. The top axis marks the spectral type.

ready known from ground-based multisite campaigns prior to the space asteroseismology era. We distinguish between β Cep multi-periodic light curves due to the presence of multiple low-order p- or g-modes and a third sub-class of hybrid pulsators with SPB components because their light curves have distinctly different shapes (Fig. 4).

We classified all 216 light curves based on their shape and the content of their periodogram into these three main classes. We find 49 (almost) mono-periodic, 126 multi-periodic, and 24 hybrid pulsators. The remaining 17 light curves show variability that does not fall into the three classes. Stankov & Handler (2005) classified the stars in their catalogue into similar categories and found a fraction 40 % of mono-periodic pulsators. However, they already expected this fraction to be lower due to unobserved low amplitude pulsations in the ground-based light curves, which have much higher noise level than the TESS space photometry. Our fraction of 24 % pulsators with one dominant oscillation mode is in agreement with this expectation.

Among the 17 stars we exclude from the β Cep sub-classes, TIC 22370803, TIC 311328485, and TIC 460977279 are likely short period eclipsing binaries mimicking a pulsation signal in the right frequency domain. We remove these stars in the subsequent analysis. TIC 234644092 might also be of this class but without compelling evidence, we kept the star in our analysis. In contrast, TIC 285370131, TIC 450383484, TIC 329992262, TIC 399436828, and TIC 410100850 show β Cep pulsations but their light curves are dominated by long-term quasi-periodic behaviour. We postulate that they are either Be stars or strongly contaminated. TIC 248275346 has additional high frequency components, which create a beating pattern unlike any other star in our sample. The three stars TIC 326815593, TIC 327282466, and TIC 365623418 are noisy and modulated with additional non-periodic variability which stems likely from flux contamination of neighbouring stars. TIC 217602397, TIC 464732844, and TIC 153657168 exhibit very noisy light curves with hidden periodic variability. Finally, TIC 406696133 is likely contaminated by a nearby, very red ($G - J = 4.3$ mag) *Gaia* long-period variable. In the TESS observations this contaminant is brighter than our target star.

The stars TIC 90964721, TIC 395218466, and TIC 1861614014 are potentially (longer-period) eclipsing binaries with β Cep pulsations, making them interesting targets for detailed modelling. The latter of the three is also included in the sample of Eze & Handler (2024).

The 199 stars in the three sub-classes are found across the whole instability region. While most of the hybrid pulsators are close or inside the overlap region of the two instability strips, we find some notable exceptions. In particular the distinct group at

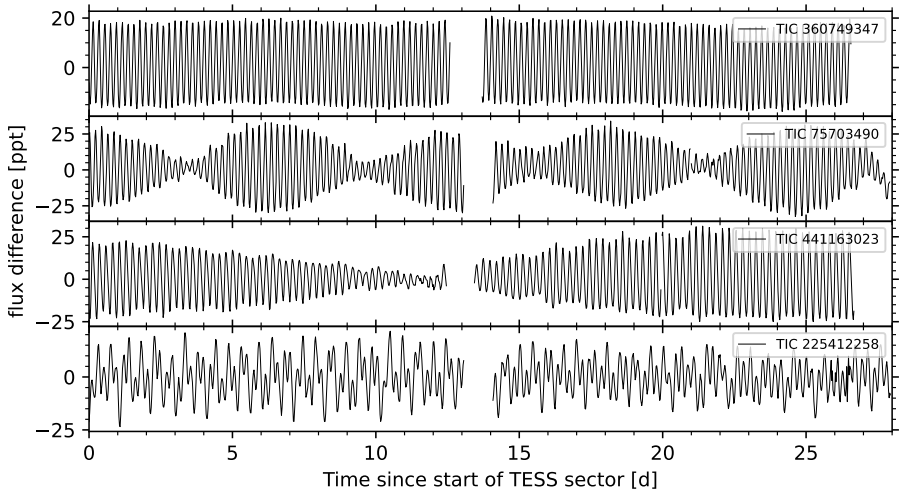

Fig. 4. Examples of single sector TESS light curves of β Cep variables of the different light curve sub-classes. The top light curve is a typical mono-periodic pulsator with a constant pulsation amplitude. The second and third rows show multi-periodic pulsators with different lengths of their beating patterns. For the third row the beating pattern is significantly longer than one TESS sector, hence, multiple TESS sectors are needed to resolve the close frequency peaks. The bottom row shows a typical SPB and β Cep hybrid pulsator. Due to the very different time scales of the main pulsation modes its light curve has a distinct shape.

high $T_{\rm eff}$ (see above), hosts two hybrid pulsators. A HRD with the stars colour-coded by the classifications is shown in the Appendix Fig. A.1.

4.2. Rotational properties

4.2.1. Surface rotation

In our sample, some stars (e.g. TIC 445256790) show regular sinusoidal modulations in their light curves that are different from the typical multi-periodic pulsational behaviour. The signal does not represent a beating pattern. Rather, the amplitude of the pulsations is constant but the light curves reveal an added sinusoidal component with a period of a few days. When comparing the typical longer variability to the above derived estimate of the rotation frequency, we find them to match. Hence, the longer-term variability is caused by rotational modulation, a feature commonly observed in high-resolution spectroscopy and high-precision photometry among the brightest β Cep stars (e.g. λ and κ Sco Uytterhoeven et al. 2004, 2005; Handler & Schwarzenberg-Czerny 2013). As such, some of the β Cep stars are higher-mass counterparts of pulsating Ap/Bp stars observed by Bowman et al. (2018).

In order to select all possible β Cep stars with rotational modulation, we searched for matching signals among the prewhitened independent frequencies and the spectroscopic rotation rate. For each star with $f_{\rm rot} \sin i$, we select the closest signal and accept it as the (provisional) rotation frequency if it satisfies $0.9 < f/f_{\rm rot} < 2.5$, allowing for $1.1 \lesssim \sin i < 0.4$ to include the unknown projection effect of the rotational axis in the line-of-sight. Given the large uncertainty on the projected rotation rate the chosen range might exclude some true rotational signals but it ensures a clean selection. Overall, we find 41 % (74/182) of our sample to show some variability within the probed range.

Most of the potential photometric rotational signals are close to the estimated $f_{\rm rot} \sin i$ indicating inclinations closer to the equator than to the pole of the rotation axis. This skewed distribution stems from two selection effects favouring $\sin i \sim 1$ above $\sin i \sim 0$. Firstly, the inclination angles of least cancellation of low-degree tesseral and sectoral modes deliver $\sin i \in [0.8, 1.0]$ (see Appendix 1 in Aerts et al. 2010, for a definition and value of these viewing angles). Moreover, for the fastest rotators the pulsation modes tend to be sectoral modes concentrated to a band around the equator, maximising the visibility of such pulsations from the equatorial region (e.g. Reese et al. 2006). Secondly, stars with low $\sin i$ fall below the detection threshold in the *Gaia* $v \sin i$ measurements and hence do not occur in the sub-sample of stars with this quantity available.

For the majority of stars, we cannot see a rotational signal in the full light curve because the beating among the pulsation modes is much stronger than the potential rotational modulation. Mono-periodic stars are the only ones for which the rotational modulation can easily be seen from the light curve. We note that the modulation in Ap and Bp stars originate in surface magnetic fields detected in spectro-polarimetry. However, the typical fraction of magnetic massive stars is less than 10 % (e.g. Grunhut et al. 2017), which is lower than the fraction of detected surface rotation signals. Hence, either the fraction of magnetic β Cep stars is larger than among non-pulsating massive stars (as suggested e.g. by Hubrig et al. 2009) or the detected signals are of different origin, such as chemical spots.

4.2.2. Influence of internal rotation on pulsations

Due to the shift between a reference frame rotating with the star and the observer's inertial reference frame, the observed pulsation frequencies of non-zonal modes get shifted with respect to their value in a frame of reference corotating with the star. We thus expect $f_{\rm l}$ and $f_{\rm rot}$ to be correlated for sectoral ($l = |m| > 0$) or tesseral ($0 > |m| > l$) modes. Depending on the mode's azimuthal order, a smaller or larger frequency shift of $m\langle\Omega\rangle$ occurs for the mode's frequency between the two reference frames, where $\langle\Omega\rangle$ is the averaged internal rotation frequency throughout the stellar interior. In general, the internal rotation of stars is not rigid and may hence differ substantially from the surface rotation $f_{\rm rot}$. Asteroseismology has shown the level of differentiality between the core, the envelope, and the surface rotation is limited to about 10% for intermediate-mass main sequence single stars with a convective core (Li et al. 2020a; Aerts 2021). However, the few β Cep stars with such measurement show a large spread in the level of their differential rotation (Burssens et al. 2023).

Figure 5 shows the main frequency observed in the TESS light curves against the estimated projected surface rotation frequency. We find a clear positive correlation between the two properties, as anticipated. We only have a (rather uncertain) direct estimate of the projected value of the surface rotation frequency in the line-of-sight, while the pulsation frequency's shift is mainly determined by the rotation in the region of the star where the mode has most of its probing power. The low-order modes in β Cep stars are dominant in the envelope and hence

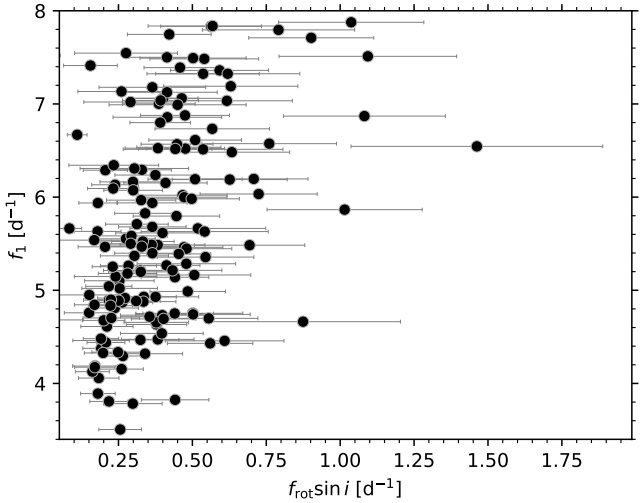

Fig. 5. Main pulsation frequency f_1 against the projected surface rotation frequency $f_{\rm rot} \sin i$ of the 162 stars with available $v \sin i$ in the *Gaia* ESP-HS data. A clear correlation between both quantities is visible. Uncertainties in the pulsation frequency are typically within the symbol size.

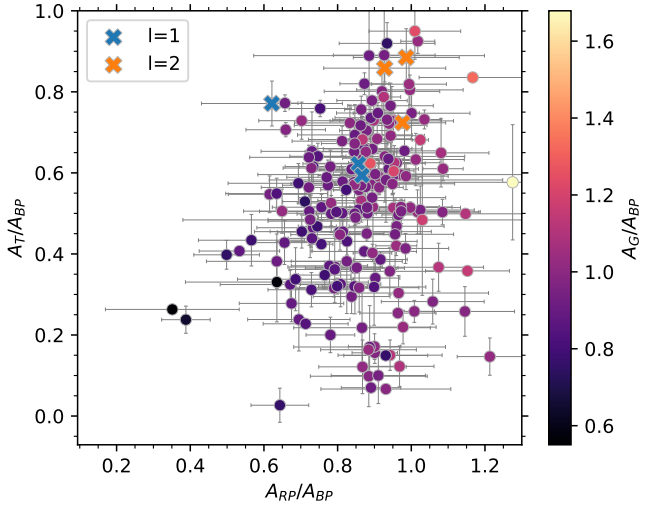

Fig. 6. Pulsation amplitude ratio $A_T/A_{\rm BP}$ against $A_{\rm RP}/A_{\rm BP}$ for the main mode detected in the *Gaia* photometry of 205 β Cep stars. The colour-coding is according to the amplitude ratio $A_G/A_{\rm BP}$. Crosses mark a few well-studied bright pulsators with secure mode identifications from the literature.

mainly probe the rotation in that region, denoted here as $\Omega_{\rm env}$. This, and the fact that the shift of any non-radial mode frequency in the line of sight is proportional to $m\Omega_{\rm env}$, implies that the main pulsation frequency f_1 is not tightly related to the projected surface rotation frequency, explaining the scatter in Fig. 5.

5. Mode identification from TESS and *Gaia* data

Identifying the degree l of at least one pulsation mode is required to reduce degeneracy and perform meaningful asteroseismic modelling of β Cep stars (Hendriks & Aerts 2019). In addition, it is also of importance to obtain an observational distribution of the mode degrees to advance our understanding of the mode selection mechanisms. Hence, we attempt to identify the pulsation modes of the *Gaia* sample to (1) learn about the distribution of pulsation modes in β Cep stars from a large sample based on space photometry, (2) provide the input for detailed future modelling of the most promising sample stars, (3) open pathways towards ensemble asteroseismology of β Cep pulsators observed across the entire sky from combined TESS and *Gaia* space data.

5.1. Multi-colour photometry

Traditionally in ground-based work, the pulsation modes of β Cep stars have been identified with either multi-colour photometry or time-resolved spectroscopy (see Introduction, Sect. 1). In multi-colour photometry the amplitude ratios are calculated from the amplitudes of the pulsation modes as measured in different photometric filters. The bluest filter is typically used as the reference filter because the pulsation amplitude in β Cep pulsators is the largest in the blue part of the spectrum. The lowest degree p-modes (i.e., radial modes with $l = 0$) show a stronger drop-off with increasing wavelength than dipole or quadrupole modes, providing information about the mode degree l (we refer to Heynderickx et al. 1994, for details of this methodology). As already discussed in Hey & Aerts (2024), the *Gaia* time series photometry offers multi-colour photometry which may help in mode identification.

Figure 6 shows amplitude ratios of the *Gaia* $G_{\rm RP}$ and TESS T band observations of stars with the same dominant pulsation frequency in *Gaia* and TESS. The ratios are computed with respect to the $G_{\rm BP}$ amplitude. In order to understand the position of different stars in this diagram and assess the feasibility of our approach, we marked the same quantities for stars with known mode identifications from the literature. As expected the quadrupole ($l = 2$) modes fall in the top right corner with amplitude ratios close to unity independent of the filter. Identified dipole ($l = 1$) modes are found at lower amplitude ratios, while we expect to find the stars with dominant radial ($l = 0$) mode in the lower left corner because their amplitudes decrease strongest with wavelength (see Heynderickx et al. 1994).

The few β Cep stars with identified modes from long-term or multi-site campaigns in the literature tend to be too bright for *Gaia*, hence no stars with known dominant radial pulsation is marked in Fig. 6. No clearly separated groups emerge from Fig. 6 in terms of the mode degree. Hence, we cannot achieve unambiguous identification from *Gaia* and TESS multi-colour amplitude ratios alone. However, the trend of having $l = 2$ in the upper right corner and $l = 1$ in the centre of the plot does emerge and is encouraging.

5.2. Search for rotationally split multiplets in the TESS data

Given the high signal-to-noise TESS light curves of these high amplitude β Cep pulsators, mode identification might also be possible from the pre-whitened pulsation frequencies in the TESS data by identifying rotationally split multiplets, following the prototypical case of HD 129929 (Aerts et al. 2003). A pulsation mode with $l > 0$ can be split into $2l + 1$ observable mode components of azimuthal order m. In the corotating frame, the offset from the $m = 0$ central mode is proportional to $\langle\Omega\rangle$ when treating the Coriolis force perturbatively up to first order (Ledoux 1951).

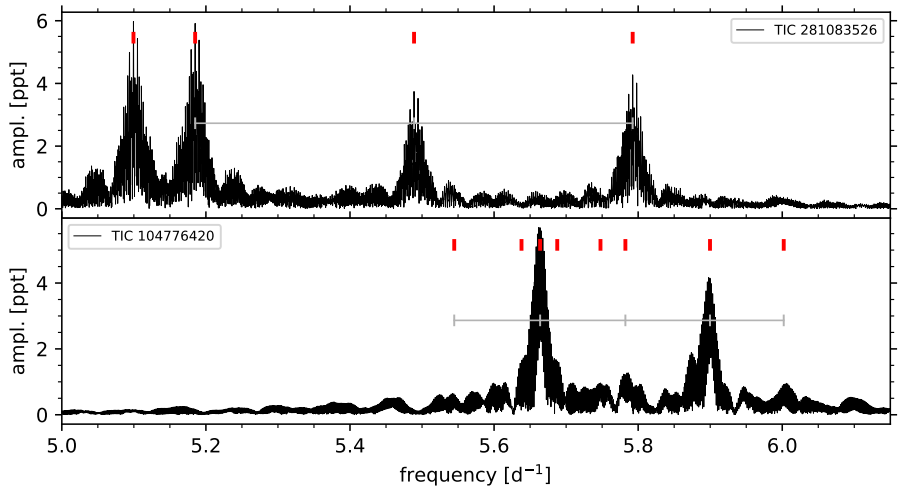

Fig. 7. Examples of rotationally split multiplets found in the amplitude spectra of the TESS data. The top panel shows an $l = 1$ mode split into three azimuthal components. The central frequency of the multiplet ($f \approx 5.5\,\mathrm{d}^{-1}$) had the dominant amplitude in the *Gaia* data. The strong peak left of the triplet corresponds is an independent mode. The bottom panel shows one of the few identified complete $l = 2$ multiplets. In both panels the splittings are marked with grey markers connected by a line. The red markers at the top of each panel indicate the extracted frequencies from pre-whitening.

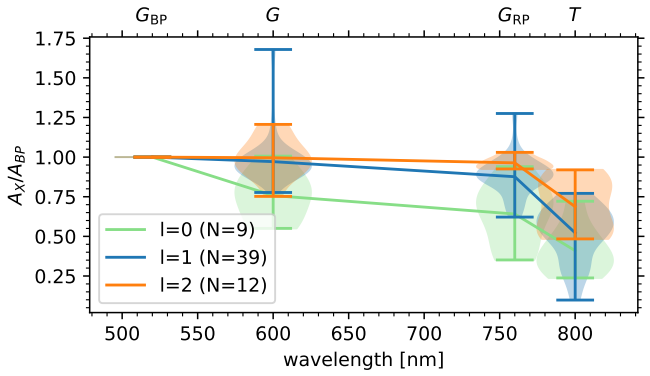

Fig. 8. Violin plots of amplitude ratios for identified pulsation modes over the filter's effective wavelengths. The lines connect the mean values for each mode degree. Radial modes ($l = 0$, green) are cleanly separated from non-radial pulsation modes ($l = 1$, blue, $l = 2$ orange), which have a larger overlap. The filter names are given at the top.

We exploited the connection between the two measurements f_1 and $f_{\mathrm{rot}} \sin i$ and the unknown $\langle\Omega\rangle$ required to find rotational multiplets, by relying on the correlation seen in Fig. 5. Up to first order in $\langle\Omega\rangle$ the splittings are symmetrical, which is a good approximation for slow to modest rotators among the β Cep pulsators. This enabled us to distinguish between chance alignments of frequency peaks and true multiplets in the periodograms.

Figure 7 shows examples of rotationally split multiplets we found in the TESS data. In total, we identified 12 incomplete and 48 complete rotational multiplets for the dominant frequency. The majority of these stars (83 %) pulsate in $l = 1$ modes and far fewer in $l = 2$ modes (17 %). However, we note that some of the potential modes are near the detection limit. Hence, only a subset of 37 of these stars with very clear splittings is used in the following analysis.

Figure 8 shows the distributions of the mode degrees identified in this way. This diagram includes only the stars for which we visually identified the pulsation modes with high certainty. For each photometric band and pulsation mode, we show the mean value of the amplitude ratio and a violin plot of the distribution. For all three considered degrees l the distributions overlap strongly, which explains why we could not find a clean separation in Fig. 6 from the *Gaia* data alone and had to work with extra information from the rotational splitting in the TESS data.

We find that the mean amplitude ratio values are distributed as expected, with a larger amplitude ratio for higher l. The radial modes show clearly smaller amplitude ratios than the non-radial modes. The distinction between $l = 1$ and $l = 2$ modes is small, following the results in Fig. 6.

5.3. Probabilistic mode identification from TESS and Gaia

With the secured mode identifications from rotational splittings in the TESS data, we now return to the *Gaia*-TESS multi-colour photometry for all pulsators, to identify the dominant mode of the stars without rotational splitting. We do so from their *Gaia* photometry following Fig. 6, after careful inspection of the position of the pulsators with rotational multiplets in this diagram.

Given the overlap of the distributions of the amplitude ratios for modes of $l = 0, 1, 2$ in Fig. 8 and the spread in Fig. 6, we aimed to estimate the mode identifications for the full sample based on a probabilistic framework including all photometric measurements and their uncertainties. To find the probability of a given mode identification under the measured *Gaia* and TESS amplitude ratios, we used the distributions shown in Fig. 8 as our training set and modelled them with a kernel density estimator (K_l). For each star, we calculated the likelihood L_l for a given mode l in a Naïve Bayesian scheme (Zhang 2004) by integrating K_l over the uncertainty interval of the measured amplitude ratios $\mathbf{A}$ of the three considered photometric bands (with σ as their uncertainties):

$$L_l = \int\int\int_{\mathbf{A}-\sigma}^{\mathbf{A}+\sigma} K_l(\mathbf{A})\mathrm{d}\mathbf{A}. \quad (1)$$

The kernel density estimators were based on 9 values for $l = 0$, 39 values for $l = 1$, and 12 values for $l = 2$.

To estimate the probability, we initially chose a flat prior but noticed that some stars with clear splittings were assigned $l = 0$. Given the high occurrence rate of $l = 1$ modes, we chose to use a non-flat prior with a weighting of 0.5 for $l = 1$ and 0.25 for the other two considered degrees.

All in all, we identified 198 mode degrees ($l = 0$: 26, $l = 1$: 145, $l = 2$: 27) with probability $p > 50$ %. For 54 stars, we found a different mode degree to be more likely than the one assigned from visual inspection. Five of these stars were in our training set. Except for TIC 436240475, our initial identification had a relatively high probability close to 50 % as these stars are located in the overlap region of the distributions of two mode degrees.

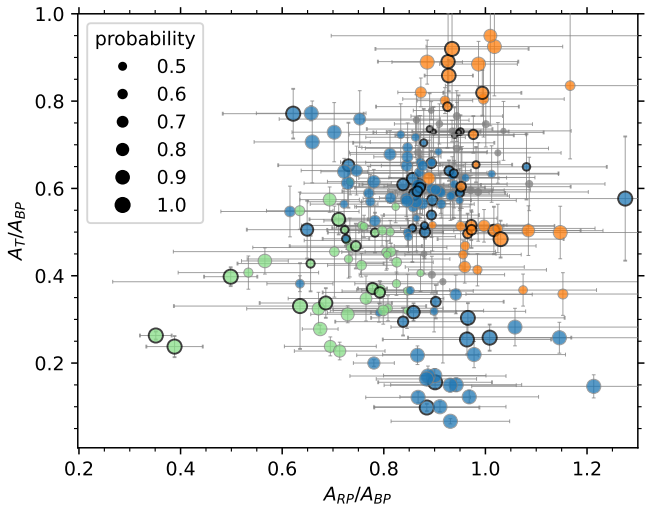

Fig. 9. Amplitude ratio diagram based on $A_{\rm RP}/A_{\rm BP}$ and $A_T/A_{\rm BP}$ similar to Fig. 6. The colour-code shows the mode degree as determined with our probabilistic framework: $l = 0$ (green), $l = 1$ (blue), $l = 2$ (orange). Grey symbols denote stars with $p < 0.5$. The symbol size is proportional to the probability of the mode identification. Stars marked with black outlines constitute the underlying sample from Fig. 8.

For reference and to inform future modelling efforts, we provide all mode identifications and their probabilities in Table 1.

As a validation of our methodology, we also reconsidered the stars with identified modes from the literature. All but one of these were assigned the correct mode degree. The exception, TIC 419354107 (BW Vul), is a very high-amplitude radial pulsator (Sterken & Jerzykiewicz 1993) whose mode also got wrongly identified from high-resolution time-series spectroscopy when relying on linear pulsation theory (Aerts et al. 1995). Its position in Fig. 6 is indeed not consistent with the expectations for a linear radial mode, which is why we had already excluded this star from that figure.

In summary, we are able to identify the dominant mode degree of 198 *Gaia* β Cep pulsators with a probability $p > 50\,\%$ based on their TESS light curve, *Gaia* multi-colour amplitude ratios, and the estimated surface rotation rates. This represents the largest sample of identified pulsation modes in β Cep stars to date and can serve as a prime sample for further and detailed asteroseismic population studies of β Cep stars. In the following, we present global seismic analyses and modelling of this homogeneously composed sample.

6. β Cep ensemble asteroseismology

To gain deeper insights in the population of the *Gaia*-observed β Cep stars, we used the identification of the dominant modes. In the following, we characterise the ensemble and subject its stars to grid modelling.

6.1. Distributions of the identified modes

The mean behaviour of the identified modes of the full sample over the wavelength is very similar to the hand-selected sample in Fig. 8. However, we find a slightly clearer separation between the two considered non-radial modes. Notably the distributions of $A_T/A_{\rm BP}$ for $l = 1, 2$ shown in Fig. A.2 are bimodal in the TESS amplitude but not in the other photometric bands.

Figure 9 shows an amplitude ratio diagram similar to Fig. 6 colour-coded by the determined mode degree. The distribution of mode degrees follows the expected distributions with $l = 2$ modes in the top right (orange) at the highest amplitude ratios. Stars with $l = 1$ as their primary mode degree are located in the central part (blue) and radial modes $l = 0$ in the lower left (green).

When going into details, we find a complicated pattern with several overlapping regions. Stars to which our algorithm assigned low probabilities in the mode identification belong to the overlapping regions between the different degrees. Due to the three dimensionality of the distributions these overlap regions create fuzzy borders in the two dimensional projection in Fig. 9. An interesting feature is the concentration of $l = 2$ modes near $A_{\rm RP}/A_{\rm BP} \approx 1$ and $A_{\rm T}/A_{\rm BP} \approx 0.5$ which is clearly separated from the main population at the top. Similarly, the group of high probability $l = 1$ modes at the bottom of Fig. 9 is disjoint from the main $l = 1$ population. These two regions create the bimodalities in the TESS amplitude ratios in Fig. A.2. From our TESS data, we find for some of these stars obvious multiplets in which the *Gaia* observed frequency (and often main TESS frequency) is not the central frequency. Hence, the multi-colour photometry also carries information on the azimuthal order m.

When placing the stars with identified modes in the HRD, we find the β Cep stars in which the radial mode is the dominant mode to be mainly of lower mass while non-radial pulsators can be observed throughout the whole β Cep mass range (c.f. Fig. A.3). Two stars with radial modes stand out due to their relatively high luminosity. Notably, the radial pulsators seem to concentrate in the later half of the main sequence in the overlap region between the β Cep and SPB instability strips.

6.2. Rotationally split multiplets and asymmetries

As introduced in Sect. 5.2, rotation can split non-radial modes into multiplets with splittings proportional to the envelope rotation rate. In Fig. 10, we show the observed splittings against the estimated surface rotation rate. As expected, a clear positive correlation between the rotation rate and the splitting is observed. Yet, we recall that β Cep stars can have strong radial differential rotation (Aerts et al. 2003; Pamyatnykh et al. 2004; Burssens et al. 2023) and the surface rotation rate may differ from the internal rotation rate at the fractional radius where the mode is most sensitive.

We also mark the absolute asymmetries (maximum difference to the mean splitting) in Fig. 10. For most of the stars this asymmetry is small, though it is pronounced for a minority. A purely rotationally split multiplet would consist of evenly and symmetrically spaced components if the Coriolis force, due to the mean envelope rotation, has only a small influence, allowing for a first-order pertubative approach. However, second order-terms are relevant for β Cep stars and include rotational deformation of the star (Saio 1981). This effect shifts the split frequencies asymmetrically with respect to the central frequency (Dziembowski & Goode 1992; Goupil et al. 2000). In addition, properties such as magnetic fields (e.g. Bugnet et al. 2021) or binarity (e.g. Guo et al. 2024) also influence the asymmetry of split multiplets, leading to asymmetries in the observed frequency spectra and enabling detailed asteroseismic inferences (e.g. Vanlaer et al., in prep.).

Table 1. Observational parameters and mode identifications. For simplicity, we omitted the uncertainties in this excerpt.

TIC	*Gaia*DR3 source ID	RA (deg.)	Dec. (deg.)	$\log T_{\rm eff}$	$\log L$	Ref.	$f_{\rm rot}\sin i$ (d^{-1})	f_1 (d^{-1})	f_{Gaia} (d^{-1})	$f_{\rm TESS}$ (d^{-1})	LC type	$a_G/a_{\rm BP}$	$a_{\rm RP}/a_{\rm BP}$	$a_T/a_{\rm BP}$	l	$p(l=0)$	$p(l=1)$	$p(l=2)$	splitting (d^{-1})	δ_A
4030832	5933776187446650880	246.18895	-53.46433	4.48	4.72	2	0.54	5.35610	5.35473	5.35610	mono	0.96	0.89	0.66	1	0.13	0.69	0.18	0.12	0.02
7038369	5933980456100089856	246.58808	-51.79895	4.35	3.93		0.19	4.46055	4.45906	4.46055	multi	0.91	0.77	0.57	1	0.30	0.67	0.03	…	…
11478661	2060836535411106304	303.93684	37.71048	4.32	4.07		0.21	6.28892	6.28626	6.28892	multi	0.57	0.64	0.33	0	1.00	0.00	0.00	…	…
11856739	5940654422886567936	247.12647	-49.35147	4.45	4.55		0.38	4.47288	4.47143	4.47288	hybrid	0.89	0.78	0.50	0	0.58	0.41	0.01	…	…
13332837	2061190956100233216	305.39636	38.61325	4.37	4.17	3, 4	0.48	6.87714	6.87450	6.87714	hybrid	0.90	0.73	0.65	1	0.13	0.83	0.04	…	…
13765605	4655100690331121152	37.40739	61.20823	4.41	4.16		0.34	4.92968	4.92960	4.92968	multi	1.18	0.95	0.73	…	0.07	0.47	0.46	0.53	-0.10
13973539	2061131715608660736	305.76197	38.45576	4.40	4.65	3	0.26	3.50524	3.50277	3.50524	hybrid	1.03	1.01	0.63	1	0.15	0.54	0.31	…	…
14085632	2057943789022547968	305.72188	37.11278	4.53	4.94		0.38	4.63305	4.63295	4.63305	multi	0.94	0.93	0.89	2	0.03	0.03	0.94	…	…
15166556	5990434159009247232	244.59709	-45.84034	4.36	3.73	2	0.76	6.57384	6.57244	6.57384	multi	1.01	0.95	0.73	…	0.27	0.35	0.38	0.20	0.03
…																				

Notes. *Ref.* indicates stars listed in other works. f_{Gaia} and amplitudes in the *Gaia* bands from Gaia Collaboration et al. (2023). The full table, including uncertainties, is available at the CDS.

References. (1) Stankov & Handler (2005); (2) Pigulski & Pojmański (2008); (3) Labadie-Bartz et al. (2020); (4) Shi et al. (2024); (5) Eze & Handler (2024).

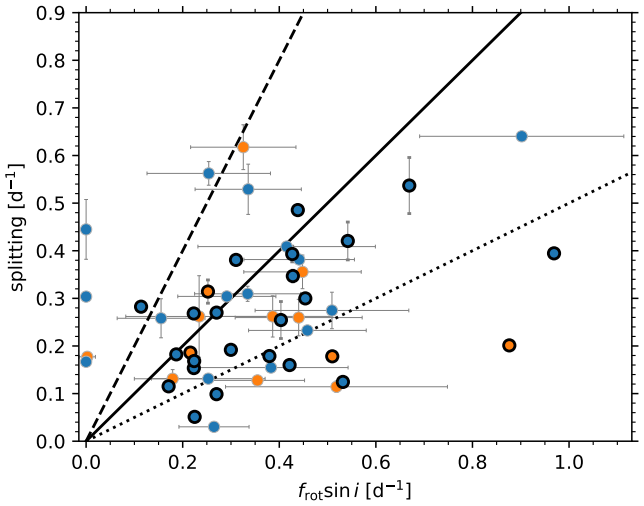

Fig. 10. Observed mode splittings against the projected surface rotation rate ($f_{\rm rot}\sin i$, thin outlines) or photometric surface rotation rate ($f_{\rm rot}$, solid outlines). The three lines show the widths of splittings equal to the surface rotation rate (solid) as well as half (dotted) and twice (dashed) the surface rotation rate. We note that the internal rotation rate at the position of maximum probing power might be different from the surface rotation. The uncertainties on the splittings indicate the maximum difference of the individual splittings to the mean splitting of the multiplet and are a measure for the asymmetry. The colours show our manual classification into $l = 1$ (blue) and $l = 2$ (orange) modes.

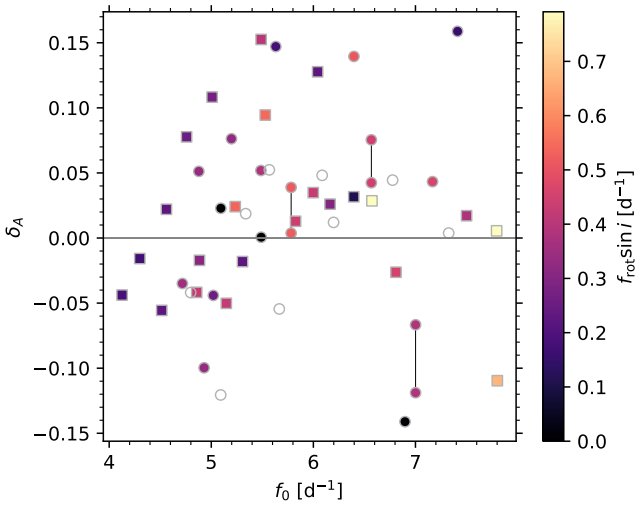

Fig. 11. Asymmetries of 48 complete rotationally split multiplets δ_A against their central frequency f_0 colour-coded by the projected surface rotation rate. Square symbols mark stars with measured photometric surface rotation rates ($f_{\rm rot}$). Symbols connected by a line belong to the same ($l = 2$) multiplet. The measurement uncertainties are within the symbol sizes.

Guo et al. (2024) (see also Goupil et al. 2000; Deheuvels et al. 2017) define the observed asymmetry as

$$\delta_A = -\frac{f_{-m} + f_{+m} - 2f_0}{f_{+m} - f_{-m}}, \quad (2)$$

with f_0 the central frequency and $f_{\pm m}$ the frequencies of azimuthal order $m = \pm 1$. In Fig. 11, we show the asymmetries for 48 stars in our sample against the central frequency f_0 of the multiplet. Most of the splittings are positive as expected for a simple rotational deformation (Guo et al. 2024). The splittings shown in Fig. 11 are only the splittings most obvious and close to the main oscillation mode. Several stars show additional splittings which will be analysed elsewhere.

Negative asymmetries in β Cep stars hint towards internal magnetic fields. Our understanding of core magnetism in massive stars is still limited (Vanlaer et al., in prep.), despite its potential impact on stellar evolution. A large sample of measured internal magnetic fields from asteroseismology would deliver constraints for evolutionary models, similarly to the recent advances in red giants (Li et al. 2023).

6.3. Modelling the population of β Cep stars

To understand the population of β Cep stars better and gain insights into the distributions of their physical properties with respect to the selected main pulsation mode, we apply grid modelling. We used the β Cep MESA stellar evolution grid presented by Burssens et al. (2020, 2023). The grid was calculated for masses between 9 $M_\odot$ and 21.5 $M_\odot$ at solar metallicity with a constant envelope mixing level fixed at $D = 1000\,{\rm cm^2\,s^{-1}}$ and an exponentially decaying diffusive core overshoot with the parameter range $0.005 \leq f_{\rm ov} \leq 0.035$. The β Cep grid mimics the effect of rotational mixing by including core overshoot and envelope mixing. For details of the physical implementation, we refer the reader to Burssens et al. (2023).

The required mode identification for the modelling is not limited to the degree l but we require the radial order n and azimuthal order m as well. All models will be fit in the azimuthal order $m = 0$ necessitating us to identify the central peak of split modes. For complete multiplets the choice is obvious. In incom-

plete multiplets, we assumed in most cases the highest peak to be the at $m = 0$. Exceptions from this rule were for example made when the highest amplitude TESS frequency does not agree with the *Gaia* frequency.

The radial order can neither be deduced directly from the observations nor from a direct fit of the model. Rather, we fitted model with the radial orders $n \in \{0, 1, 2\}$ for radial pulsators and $n \in \{-2, -1, 0, 1, 2\}$ for non-radial modes[2] using a χ^2 minimisation over $\log T_{\rm eff}$, $\log L$, and f_0. In principle, the radial order can be larger but higher order modes have not been securely established in β Cep stars, hence we did not probe them.

Stars without a model within the 1σ uncertainty ellipse (for which Δf_0 was inflated to $0.5\,{\rm d}^{-1}$, see below) were excluded from the subsequent analysis, reducing the number of modelled stars to 164. For each star, we chose the best fitting model for each n and compared the position of its modes to the observed frequency spectra. Our focus laid on the relative positions of the main pulsation mode and other visible modes with respect to the fitted model. In most but not all cases our choice of n coincides with the lowest χ^2 value among the set of best fitting models. We show one illustrative example for the identification in Appendix B, including a detailed reasoning for our choice of n.

We find the majority of the radial pulsators to pulsate in their fundamental mode (27 out of 36 modelled radial pulsators). Seven radial pulsators pulsate in their first overtone and two stars are likely second overtone pulsators. A similar picture emerges for the 128 non-radial pulsators. The dominant pulsation mode in 72 stars is the p_1 mode ($n = 1$) and 38 pulsate in g_1 ($n = -1$). Only 21 stars pulsate in their second-order mode with 18 identified p_2 and three g_2 pulsators. The remaining seven stars are likely f-mode pulsators.

For the final model selection and uncertainty estimation, we employed a MCMC approach with a χ^2 merit function, similar to our work in Fritzewski et al. (2024), to which we refer for details. Since we rely on a grid of stellar models with fixed input physics on some aspects (notably the level of envelope mixing, where the low-order modes have dominant probing power), we allow for an overall mismatch between observed and fitted frequencies (see Aerts et al. 2018, for an extensive discussion in the case of g modes). In order to encapsulate this theoretical uncertainty caused by the fixed yet uncertain input physics adopted in the model grid, we include an artificially inflated frequency uncertainty of $0.5\,{\rm d}^{-1}$. This procedure allows us to recognise correspondence between the observed and predicted frequency pattern of the low-order modes and thus encapsulates any systematic frequency shifts between the model predictions and the observed frequency f_0 (cf. the procedure explained in in Appendix B).

The histograms in Fig. 12 show distributions of the obtained masses, normalised core hydrogen fraction (X_c'), age, relative convective core mass, radius, and horizontal versus radial displacement of the dominant mode. As expected from the distribution of β Cep stars in the HRD in Fig. 3, the number of β Cep stars declines with mass, with most β Cep stars found in the range $9 \leq M_{\rm ini}/M_\odot \leq 13$. In agreement with Fig. A.3, radial pulsators are mostly found among the lower mass β Cep stars.

The distribution of X_c' shows more structure in particular when focusing on the pulsation degree. Radial pulsators are constrained to the central region of the probed core hydrogen fraction, while non-radial pulsators can be found over the whole range. Notably the quadrupole pulsators follow a bimodel dis-

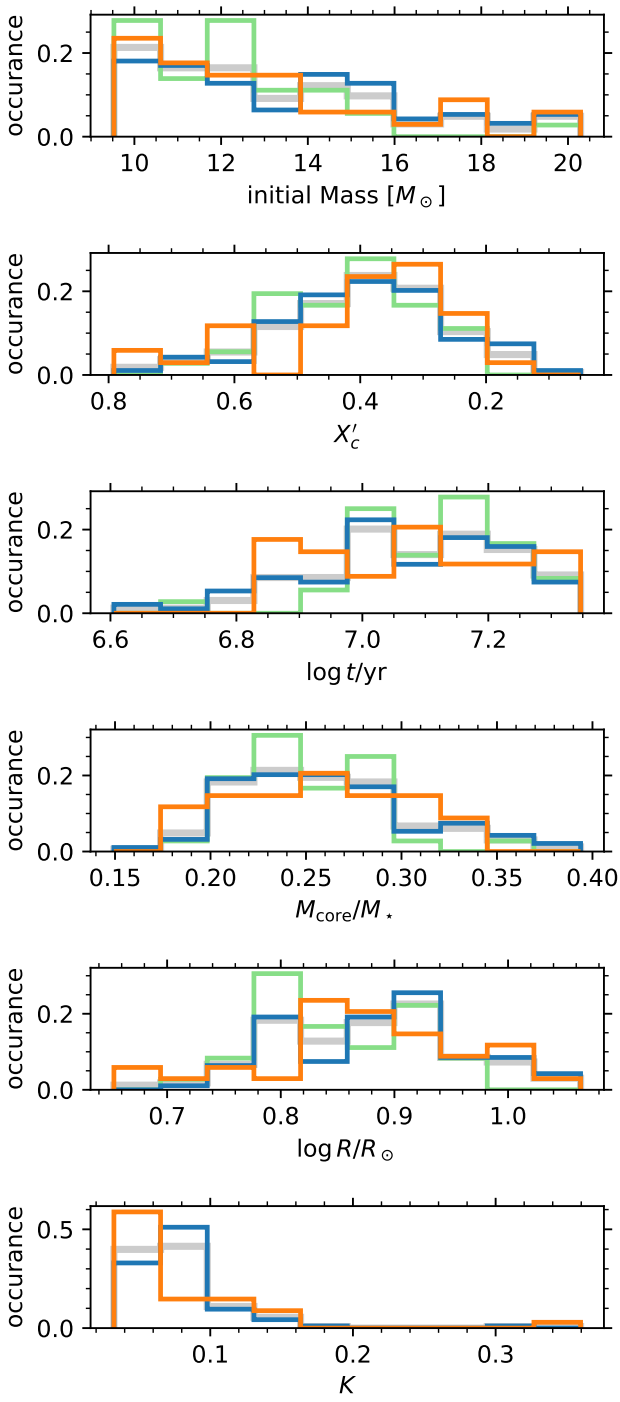

Fig. 12. Distribution of β Cep parameters for the modelled stars. Each panel contains the histograms for the full sample (grey) and degree $l = 0$ (green), $l = 1$ (blue), and $l = 2$ (orange). The histograms are normalised to the number of stars within the group. The mass distribution in the top panel shows that the majority of stars are found in the lower-mass end of the instability strip. The second panel gives the distribution of the normalised core hydrogen fraction X_c'. We find the majority of stars in the second half of their main sequence lifetime. We note the inverted x-axis representing evolutionary stage. The middle panel shows the actual stellar age distribution. The fractional mass of the convective core in the fourth panel shows a concentration for lower core masses in agreement with the top panel and the HRDs in this work. The radius distribution in the penultimate panel is peaked at intermediate radii. The K-values in the bottom panel show the dipole and quadrupole modes to have dominant radial over tangential displacements at the stellar surface.

[2] The f-mode ($n = 0$) only exists for $l = 2$ as the frequency goes to zero for dipole modes (Takata 2012).

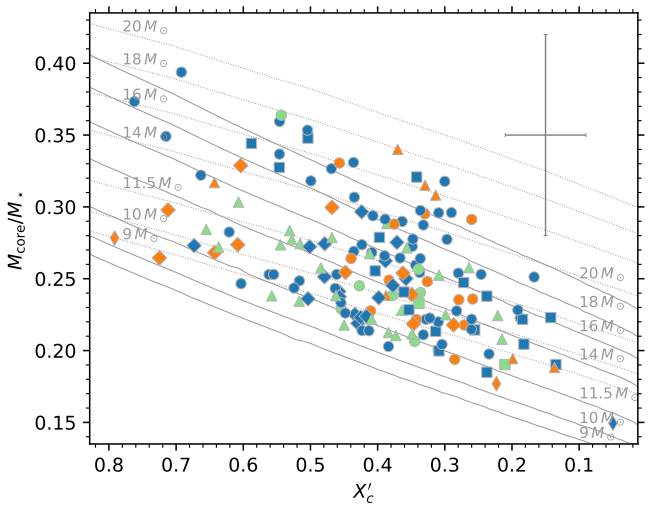

Fig. 13. Normalised convective core mass M_{core}/M_{ini} over the normalised core hydrogen mass fraction X_c'. The stars are colour-coded by their primary degree: $l = 0$ (green), $l = 1$ (blue), and $l = 2$ (orange). The shape depends on the radial order. The g modes are indicated by diamonds. We use thin diamonds for g_2 modes and wider ones for g_1 modes. Radial fundamental modes are shown with triangles; $n = 1$ of both radial and non-radial nature are indicated by circles and $n = 2$ modes by squares. The grey tracks in the background show the evolution for the indicated masses with $f_{ov} = 0.005$ (solid, labelled at low X_c') and $f_{ov} = 0.035$ (dashed, labelled at high X_c'). We note the inverted x-axis to represent the evolutionary stage. The typical uncertainty is indicated in the upper right corner.

tribution with a deficiency near $X_c' = 0.5$. This may be connected to the phenomenon of avoided crossings for such modes in the evolved stages, in line with the findings by Mazumdar et al. (2006) for the evolved β Cep star β CMa. The stellar ages do not follow the same distribution but are similarly distributed for all three pulsation degrees.

We do not show a distribution of the core overshoot because most of the stars are modelled with $f_{ov} \approx 0.02$, which corresponds to the central value in the grid. Yet, the uncertainties span the whole range of f_{ov} covered by the grid, which can be explained by the limited sensitivity of the observed modes to the near-core region and the occurrence of degeneracies between the mass, metallicity, and core overshoot when relying on just one mode (e.g., Ausseloos et al. 2004). The estimated core overshoot values result in a value for the mass-normalised convective mass ($M_{core}/M_\star$). This inferred parameter is the more interesting quantity from a stellar evolution point of view and it is a function of both the luminosity and age. The majority of stars has a value in the range $0.2 \leq M_{core}/M_\star \leq 0.3$. The few stars with a relatively high convective core mass belong to the higher-mass young O-stars well separated in the HRD (cf. Fig. 3).

To unravel the correlation between the convective core mass and the core hydrogen fraction, we show these two parameters in Fig. 13. The overall distribution shows clearly the distinction between stars with $M_{core}/M_\star \leq 0.3$ and these with more massive convective cores. The stars with higher relative core masses are typically more massive and younger as expected from stellar evolution theory. As seen from the evolutionary tracks of different masses, only the lowest mass β Cep stars can be found among full breadth of the main sequence evolution, a consequence of the position of the instability strip lying closer to the zero-age main sequence for these stars. Notably, the bimodality

Table 2. Modelled properties of the β Cep sample.

TIC	*Gaia*DR3 source ID	X_c'	M_{ini} ($M_\odot$)	log t	M_{core}/M
4030832	5933776187446650880	0.47	17.94	6.85	0.327
7038369	5933980456100089856	0.46	10.16	7.18	0.241
11478661	2060836535411106304	0.21	10.27	7.31	0.190
11856739	5940654422886567936	0.39	15.83	6.96	0.288
13332837	2061190956100233216	0.52	11.23	7.13	0.249
13765605	465510069033121152	0.48	11.50	7.12	0.251
13973539	2061131715608660736	0.17	15.75	7.04	0.251
14085632	2057943789022547968	0.37	20.29	6.84	0.340
15166556	5990434159009247232	0.72	9.65	7.07	0.265
...					

Notes. The full table, including uncertainties, is available at the CDS.

in X_c' for quadrupole pulsators is present for all masses but most pronounced in the lower mass range. In particular the younger quadrupole pulsators are low-order g-mode pulsators, while their older counterparts are a mix of g- and p-mode pulsators.

As a final distribution, we show in the bottom panel the distribution for the so-called $K-$value, defined as $K \equiv GM/(2\pi f_0)^2 R^3$, for the non-radial modes. This dimensionless quantity is connected with the boundary conditions for the pulsation equations (Aerts et al. 2010, Chapter 3). In the case of non-radial modes, it represents the ratio between the horizontal and radial displacement of the fluid elements at the stellar surface caused by the mode (as this ratio is zero for radial modes, these are not included in the bottom panel of the figure). This parameter has high values above unity (typically between 10 and 100) for high-order g modes of observed SPB stars (De Cat & Aerts 2002), as their modes dominantly cause horizontal displacements. Here, as expected for low-order modes, we find the opposite with dominantly radial displacements but with non-negligible contributions from horizontal motions. The values for K range from about 0.03 to about 0.2 for the dominant mode of most of the *Gaia* β Cep stars in our sample.

In summary, we successfully modelled 164 β Cep stars with a grid modelling approach and provide distributions of their masses, ages, convective core masses, radii. As such, these distribution provide a first insight into the properties of the population of β Cep stars. Of particular interest for future investigations on the mode excitation of this population is the connection between the stellar age and the degree of the dominant mode, if any. We give the best fitting model properties in Table 2. A discussion of the accuracy of the asteroseismic parameters in comparison with the input values from *Gaia* can be found in Appendix C.1.

6.4. Period-luminosity relations

The radial fundamental and low-order p-modes probe the stellar mean density. For a given type of pulsator this translates into a dependency of the frequency on the luminosity. In earlier works on β Cep stars several authors attempted to find a period-luminosity relation (e.g. Blaauw & Savedoff 1953; Jakate 1980; Waelkens 1981) similar to the one in Cepheid variables (Leavitt & Pickering 1912). However, the uncertain mode identifications led to a large scatter in these relations (see review by Lesh & Aizenman 1978).

As we now possess complete mode identifications of tens of β Cep stars, we can select the stars pulsating in modes that probe the mean density and fit a period luminosity relations to them. In Fig. 14, we show them in the log P-log $L/L_\odot$ plane colour coded by their mode degree. Using a linear regression, we arrive at a

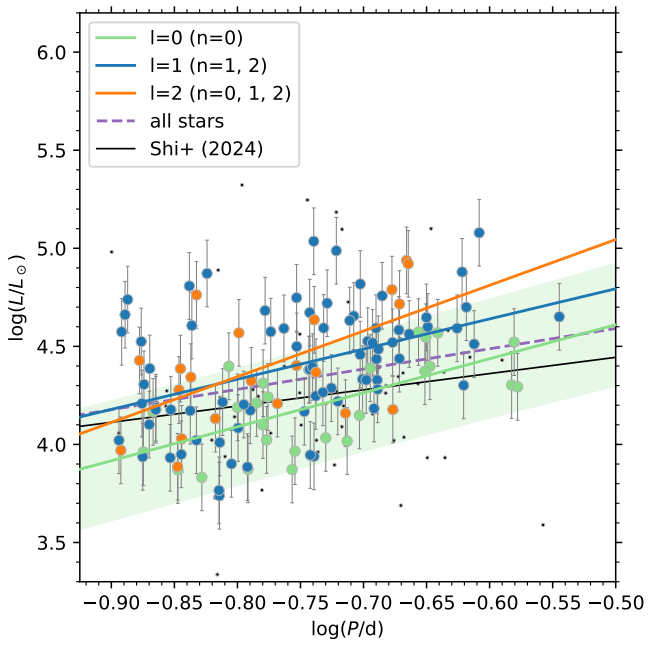

Fig. 14. Period luminosity relations for modes of different degrees ($l = 0$ (green), $l = 1$ (blue), and $l = 2$ (orange)). The period luminosity relations include only the radial fundamental mode ($n = 0$) for radial modes and p-modes for non-radial modes. The black line shows the relation from Shi et al. (2024) fitted to their whole sample. For comparison, we show a similar period-luminosity relation for our sample in purple (dashed). For clarity, we show the uncertainty interval only for the radial pulsators. The period-luminosity relation for dipole p-mode pulsators has a similar uncertainty band while it is larger for the quadrupole pulsators. The small black data points in background shows dominant g-mode and higher-order radial pulsators excluded from the fits.

period luminosity relation for each set of pulsators:

$$\log L/L_\odot = (1.73 \pm 0.41) \log P + (5.5 \pm 0.30) \quad (l = 0) \tag{3}$$
$$\log L/L_\odot = (1.54 \pm 0.39) \log P + (5.6 \pm 0.29) \quad (l = 1) \tag{4}$$
$$\log L/L_\odot = (2.33 \pm 0.75) \log P + (6.2 \pm 0.59) \quad (l = 2) \tag{5}$$

with P as the mode period in days.

We find the three relations to be stacked by their mode degree, such that the lowest degree modes (radial) follow a period-luminosity relation with the lowest luminosity for a given period. The relation for the quadrupole modes intersects with the relation for the dipolar modes likely due to fewer stars in the sample and larger uncertainty on its parameters. Shi et al. (2024) recently provided a similar period-lumionsity relation for their sample of β Cep stars. In comparison to a linear regression of all stars 155 from Shi et al. (2024) regardless of their mode degree, our period-luminosity relations are slightly steeper. When including all stars of our sample, we find a similar slope, highlighting the importance of mode identification for period luminosity relations.

6.5. Average envelope rotation

Radial differential rotation was observed in the handful of β Cep stars with a measurement of the internal rotation (e.g. Aerts et al. 2003; Pamyatnykh et al. 2004; Dziembowski & Pamyatnykh 2008; Burssens et al. 2023, Vanlaer in prep.). Based on the observed splittings (Sect. 5.2) and our modelling results for the

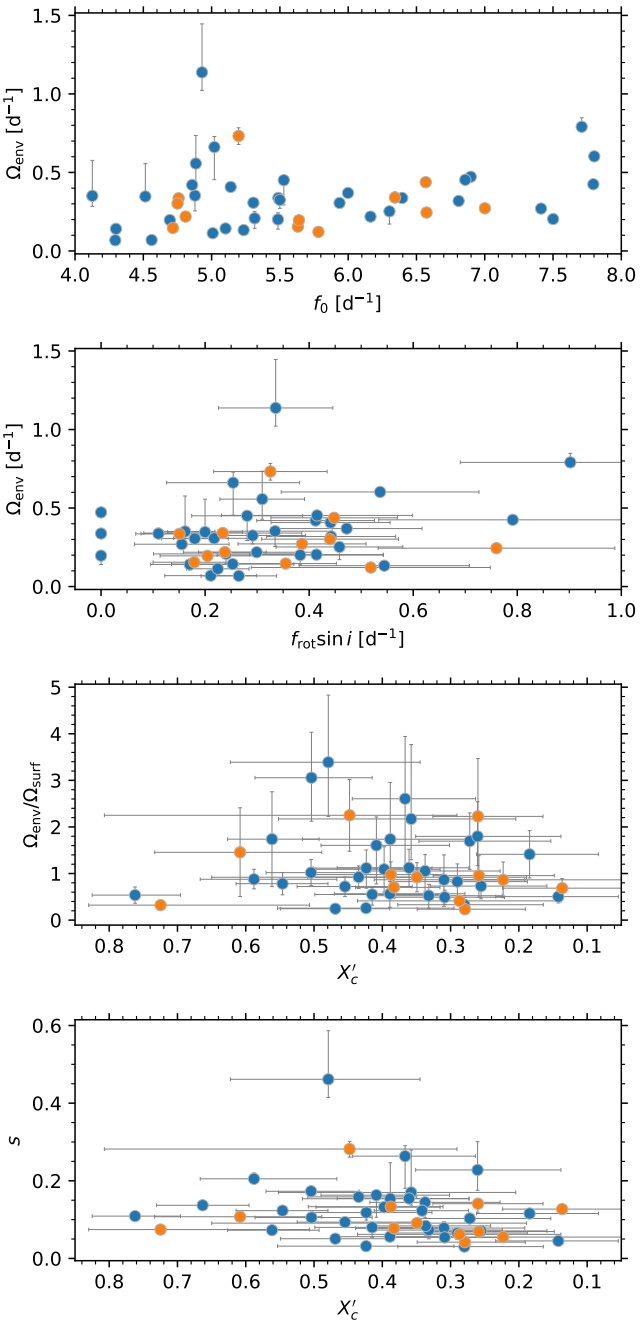

Fig. 15. Envelope rotation $\Omega_{\rm env}$ and derived parameters against observed frequencies and estimated core hydrogen fractions for 48 stars. The top panel shows the envelope rotation rate against the zonal mode frequency of the multiplet (f_0) and the second panel against the projected surface rotation rate $f_{\rm rot} \sin i$. The third and fourth panel show derived rotational properties against the evolutionary stage. In the former, we show an upper limit for the level of differential rotation ($\Omega_{\rm env}/\Omega_{\rm surf}$) and in the bottom panel the spin parameter (s) of the mode in the envelope. The colour-code corresponds to the mode degree: $l = 1$, blue and $l = 2$ orange

Gaia β Cep stars, we calculated the internal envelope rotation rate $\Omega_{\rm env}$ from the Ledoux constant (Ledoux 1951) for the best grid model for the star. This rotation rate then also allows us to calculate the level of differential rotation between the envelope and the surface for stars with a measured $f_{\rm rot} \sin i$, as well as the spin parameter of the mode.

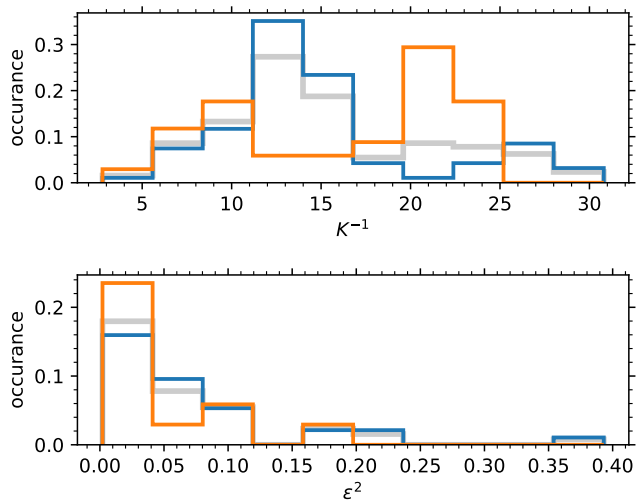

Fig. 16. Histograms of the inverse of the K-value (top) representing the importance of the 2nd-order Coriolis force versus the centrifugal force in the treatment of the pulsations and ϵ^2 (bottom) giving the influence of the centrifugal force with respect to gravity.

In Fig. 15, we show the estimated $\Omega_{\rm env}$ and derived parameters. Unlike the observed projected surface rotation and as expected, the envelope rotation deduced from the modelling does not have any correlation with the pulsation frequency of the zonal mode, as f_0 is unaffected by $\Omega_{\rm env}$ when treating the rotation perturbatively and only up to first order as we do here (top panel). The highest envelope rotation rate is not found for the fastest surface rotators but for intermediately-fast rotating stars, reflecting the effect of the unknown factor sin i and/or differential rotation between the envelope and the surface (second panel). This is visually represented in the third panel of Fig. 15, which shows the level of differential rotation assuming an almost equator-on view (sin $i \simeq 1$). This lower limit of the true surface rotation frequency is denoted here as $\Omega_{\rm surf}$. It is used to estimate an upper limit for the differential rotation between envelope and surface, which is plotted against the evolutionary stage X_c'. Aside from the projection effect, we find the most differential rotators to have an internal rate that is below four times the surface rotation. This is completely in line with the first such measurement ever done for a β Cep star (Aerts et al. 2003), which relied on rotational splitting of both a dipole and quadrupole mode. Yet, the majority of stars reveal $\Omega_{\rm env}/\Omega_{\rm surf}$ below 2. Hence, despite the few cases of strong radial differential rotation as summarised by Burssens et al. (2023), the majority of β Cep stars have a level of envelope-to-surface rotation between 0.2 and 2.

We also present the spin-parameter, s, of the dominant mode as a function of X_c'. The spin parameter is defined here as $s \equiv 2\Omega_{\rm env}/f_0$ and characterises the regime in which the pulsation mode occurs (Aerts & Tkachenko 2024). All the *Gaia* β Cep stars have their dominant mode in the super-inertial regime defined by $s < 1$. Noticably, the star with the largest spin parameter (TIC 13765605) also has the highest level of differential rotation and is about halfway its main-sequence phase.

Finally, we show in Fig. 16 histograms of the dimensionless quantities $\epsilon^2 \equiv (2\pi\Omega_{\rm env})^2 R^3/GM$ and $(2\pi f_0)^2 R^3/GM$, following Goupil et al. (2000). The latter quantity is the inverse of K already introduced above. It represents an assessment of the importance of the centrifugal force with respect to the 2nd-order Coriolis force in the treatment of the pulsations, while the former evaluates the effect of the centrifugal force with respect to gravity. Goupil et al. (2000) reported the centrifugal force (and hence the stellar oblateness) to be more important for the computation of the p-modes of rapidly rotating δ Sct stars compared to the 2nd-order rotational effect caused by the Coriolis force. Here, we provide the distributions of both ϵ^2 and K^{-1} for our population of *Gaia* β Cep stars. While their mode frequencies are in general lower than those of δ Sct stars, we still find the second-order Coriolis force to be less important than the centrifugal force for the computation of the dominant modes of the *Gaia* β Cep stars, but the difference in importance between the two forces is smaller than for δ Sct stars. We observe a bimodal distribution for the modes in the β Cep population, showing that the $l = 2$ modes have higher dependence on the centrifugal deformation than the $l = 1$ modes.

7. Conclusions

We analysed the TESS light curves of 216 *Gaia* discovered β Cep stars (Gaia Collaboration et al. 2023), including 145 new detections. By placing these stars in a *Gaia* HRD, we confirmed that all of the stars are late O or early B stars near the β Cep instability region. Yet, a detailed light curve analysis shows that at least three stars are short period eclipsing binaries. By categorising the TESS light curves, we find the majority of β Cep stars in our sample to be multi-periodic.

The combination of the *Gaia* and TESS time series photometry, allowed us to determine the mode degrees for 198 stars in our sample from their amplitude ratios. Most observed β Cep stars pulsate in non-radial modes with $l = 1$. Our identified modes constitute the largest set of identified modes of β Cep stars available to date.

From the TESS light curves, we found 60 rotationally split multiplets accompanying the main pulsation mode. The majority of these multiplets have positive asymmetries in their splittings. Yet, several stars show negative asymmetries and are prime targets for detailed follow-up analyses. We provide the first distributions of the envelope rotation rates and of upper limits for the level of differential rotation for a meaningful sample of β Cep stars. We find that most stars have envelope-to-surface rates less than 2 and many of them rotate almost rigidly. We do point out that our sample only consists of β Cep stars with a dominant mode in the super-inertial regime and thus lacks representation of the fastest rotating class members due to our sample selection from *Gaia*.

Further, we model 164 stars based on the grid calculated by Burssens et al. (2023). We provide distributions in age, convective core mass, and mass in order to inform population studies of β Cep stars. We find the $l = 2$ mode pulsators to be distributed bimodality with respect to the core hydrogen fraction and the radial mode pulsators to occur mostly in the intermediate main-sequence stage. The period-luminosity relations for the different mode degrees are steeper than one obtained for the whole ensemble.

With the upcoming *Gaia* data releases and the on-going TESS mission our approach will likely be applicable to the majority of known and still to be discovered β Cep stars. But even with the current data, expanding our work to all known β Cep stars by searching for lower amplitude pulsations in the *Gaia* data is possible. Identifying, the majority of main modes in β Cep stars will further improve our understanding of β Cep stars from a population point-of-view while delivering the highly needed input to ensemble forward modelling. Complementary to our

photometric analysis of fainter β Cep stars, the upcoming CubeSpec mission (Raskin et al. 2018; Bowman et al. 2022) will target bright β Cep stars with high-resolution time series spectroscopy from space to determine their pulsation modes to revive studies of massive pulsators and unlock their full asteroseismic potential.

Acknowledgements. We thank Tim Bedding, Siemen Burssens, Joris De Ridder, Zhao Guo, Luc IJspeert, Kalarickal Sreenivas, and Vincent Vanlaer for useful discussions. The research leading to these results has received funding from the KU Leuven Research Council (grant C16/18/005: PARADISE). CA and MV acknowledge financial support from the European Research Council (ERC) under the Horizon Europe programme (Synergy Grant agreement N°101071505: 4D-STAR). While partially funded by the European Union, views and opinions expressed are however those of the author(s) only and do not necessarily reflect those of the European Union or the European Research Council. Neither the European Union nor the granting authority can be held responsible for them. This research has made use of NASA's Astrophysics Data System Bibliographic Services and of the SIMBAD database and the VizieR catalogue access tool, operated at CDS, Strasbourg, France. This paper includes data collected by the TESS mission. Funding for the TESS mission is provided by the NASA's Science Mission Directorate. This work has made use of data from the European Space Agency (ESA) mission *Gaia* (`https://www.cosmos.esa.int/gaia`), processed by the *Gaia* Data Processing and Analysis Consortium (DPAC, `https://www.cosmos.esa.int/web/gaia/dpac/consortium`). Funding for the DPAC has been provided by national institutions, in particular the institutions participating in the *Gaia* Multilateral Agreement.
Software: This work made use of `Topcat` (Taylor 2005). This research made use of `Lightkurve`, a Python package for Kepler and TESS data analysis (Lightkurve Collaboration et al. 2018). This research made use of the following `Python` packages: `corner` (Foreman-Mackey 2016); `emcee` (Foreman-Mackey et al. 2013); `IPython` (Pérez & Granger 2007); `MatPlotLib` (Hunter 2007); `NumPy` (Harris et al. 2020); `Pandas` (McKinney 2010); `SciPy` (Virtanen et al. 2020); `scikit-learn` (Pedregosa et al. 2011).

References

Aerts, C. 2021, Reviews of Modern Physics, 93, 015001
Aerts, C., Christensen-Dalsgaard, J., & Kurtz, D. W. 2010, Asteroseismology, Springer-Verlag Heidelberg
Aerts, C., De Cat, P., Handler, G., et al. 2004a, MNRAS, 347, 463
Aerts, C., de Pauw, M., & Waelkens, C. 1992, A&A, 266, 294
Aerts, C., Marchenko, S. V., Matthews, J. M., et al. 2006, ApJ, 642, 470
Aerts, C., Mathias, P., Van Hoolst, T., et al. 1995, A&A, 301, 781
Aerts, C., Mathis, S., & Rogers, T. M. 2019, ARA&A, 57, 35
Aerts, C., Molenberghs, G., & De Ridder, J. 2023, A&A, 672, A183
Aerts, C., Molenberghs, G., Michielsen, M., et al. 2018, ApJS, 237, 15
Aerts, C., Thoul, A., Daszyńska, J., et al. 2003, Science, 300, 1926
Aerts, C. & Tkachenko, A. 2024, A&A, in press, in press
Aerts, C., Waelkens, C., Daszyńska-Daszkiewicz, J., et al. 2004b, A&A, 415, 241
Aerts, C., Waelkens, C., & de Pauw, M. 1994, A&A, 286, 136
Ausseloos, M., Scuflaire, R., Thoul, A., & Aerts, C. 2004, MNRAS, 355, 352
Balona, L. A., Pigulski, A., De Cat, P., et al. 2011, MNRAS, 413, 2403
Baran, A. S. & Koen, C. 2021, Acta Astron., 71, 113
Belkacem, K., Samadi, R., Goupil, M.-J., et al. 2009, Science, 324, 1540
Bellinger, E. P., de Mink, S. E., van Rossem, W. E., & Justham, S. 2024, ApJ, submitted, arXiv:2311.00038
Blaauw, A. & Savedoff, M. P. 1953, Bull. Astron. Inst. Netherlands, 12, 69
Bowman, D. M. 2020, Frontiers in Astronomy and Space Sciences, 7, 70
Bowman, D. M., Buysschaert, B., Neiner, C., et al. 2018, A&A, 616, A77
Bowman, D. M., Vandenbussche, B., Sana, H., et al. 2022, A&A, 658, A96
Brasseur, C. E., Phillip, C., Fleming, S. W., Mullally, S. E., & White, R. L. 2019, Astrocut: Tools for creating cutouts of TESS images, Astrophysics Source Code Library, record ascl:1905.007
Briquet, M., Aerts, C., Baglin, A., et al. 2011, A&A, 527, A112
Briquet, M., Lefever, K., Uytterhoeven, K., & Aerts, C. 2005, MNRAS, 362, 619
Briquet, M., Morel, T., Thoul, A., et al. 2007, MNRAS, 381, 1482
Briquet, M., Neiner, C., Aerts, C., et al. 2012, MNRAS, 427, 483
Bugnet, L., Prat, V., Mathis, S., et al. 2021, A&A, 650, A53
Burssens, S., Bowman, D. M., Michielsen, M., et al. 2023, Nature Astronomy, 7, 913
Burssens, S., Simón-Díaz, S., Bowman, D. M., et al. 2020, A&A, 639, A81
Cantat-Gaudin, T., Anders, F., Castro-Ginard, A., et al. 2020, A&A, 640, A1
Creevey, O. L., Sordo, R., Pailler, F., et al. 2023, A&A, 674, A26
Daszyńska-Daszkiewicz, J., Szewczuk, W., & Walczak, P. 2013, MNRAS, 431, 3396
Daszyńska-Daszkiewicz, J. & Walczak, P. 2010, MNRAS, 403, 496
De Cat, P. & Aerts, C. 2002, A&A, 393, 965
De Ridder, J., Telting, J. H., Balona, L. A., et al. 2004, MNRAS, 351, 324
Degroote, P., Briquet, M., Catala, C., et al. 2009, A&A, 506, 111
Deheuvels, S., Ouazzani, R. M., & Basu, S. 2017, A&A, 605, A75
Desmet, M., Briquet, M., Thoul, A., et al. 2009, MNRAS, 396, 1460
Dupret, M. A., Thoul, A., Scuflaire, R., et al. 2004, A&A, 415, 251
Dziembowski, W. A. & Goode, P. R. 1992, ApJ, 394, 670
Dziembowski, W. A. & Pamiatnykh, A. A. 1993, MNRAS, 262, 204
Dziembowski, W. A. & Pamyatnykh, A. A. 2008, MNRAS, 385, 2061
Eze, C. I. & Handler, G. 2024, arXiv e-prints, arXiv:2403.12281
Fabry, M., Marchant, P., Langer, N., & Sana, H. 2023, A&A, 672, A175
Fabry, M., Marchant, P., & Sana, H. 2022, A&A, 661, A123
Foreman-Mackey, D. 2016, The Journal of Open Source Software, 1, 24
Foreman-Mackey, D., Hogg, D. W., Lang, D., & Goodman, J. 2013, PASP, 125, 306
Fouesneau, M., Frémat, Y., Andrae, R., et al. 2023, A&A, 674, A28
Fritzewski, D. J., Aerts, C., Mombarg, J. S. G., Gossage, S., & Van Reeth, T. 2024, A&A, 684, A112
Frost, E. B. 1906, ApJ, 24, 259
Gaia Collaboration, De Ridder, J., Ripepi, V., et al. 2023, A&A, 674, A36
Garcia, S., Van Reeth, T., De Ridder, J., et al. 2022, A&A, 662, A82
Gautschy, A. & Saio, H. 1993, MNRAS, 262, 213
Goupil, M. J., Dziembowski, W. A., Pamyatnykh, A. A., & Talon, S. 2000, in Astronomical Society of the Pacific Conference Series, Vol. 210, Delta Scuti and Related Stars, ed. M. Breger & M. Montgomery, 267
Grunhut, J. H., Wade, G. A., Neiner, C., et al. 2017, MNRAS, 465, 2432
Guo, Z., Bedding, T. R., Pamyatnykh, A. A., et al. 2024, MNRAS, submitted, arXiv:2406.15678
Guthnick, P. 1913, Astronomische Nachrichten, 196, 357
Handler, G., Jerzykiewicz, M., Rodríguez, E., et al. 2006, MNRAS, 365, 327
Handler, G. & Schwarzenberg-Czerny, A. 2013, A&A, 557, A1
Handler, G., Shobbrook, R. R., & Mokgwetsi, T. 2005, MNRAS, 362, 612
Handler, G., Shobbrook, R. R., Uytterhoeven, K., et al. 2012, MNRAS, 424, 2380
Harris, C. R., Millman, K. J., van der Walt, S. J., et al. 2020, Nature, 585, 357
Hendriks, L. & Aerts, C. 2019, PASP, 131, 108001
Henneco, J., Schneider, F. R. N., Hekker, S., & Aerts, C. 2024, A&A, accepted, arXiv:2406.14416
Hey, D. & Aerts, C. 2024, A&A, in press, arXiv:2405.01539
Heynderickx, D., Waelkens, C., & Smeyers, P. 1994, A&AS, 105, 447
Hubrig, S., Briquet, M., De Cat, P., et al. 2009, Astronomische Nachrichten, 330, 317
Hunt, E. L. & Reffert, S. 2023, A&A, 673, A114
Hunter, J. D. 2007, Computing in Science & Engineering, 9, 90
IJspeert, L. W., Tkachenko, A., Johnston, C., et al. 2024, arXiv e-prints, arXiv:2402.06084
Jakate, S. M. 1980, A&A, 84, 374
Kass, R. E. & Raftery, A. E. 1995, Journal of the American Statistical Association, 90, 773
Kounkel, M., Covey, K., & Stassun, K. G. 2020, AJ, 160, 279
Kurtz, D. W. 2022, ARA&A, 60, 31
Labadie-Bartz, J., Handler, G., Pepper, J., et al. 2020, AJ, 160, 32
Leavitt, H. S. & Pickering, E. C. 1912, Harvard College Observatory Circular, 173, 1
Ledoux, P. 1951, ApJ, 114, 373
Lehmann, H., Tkachenko, A., Semaan, T., et al. 2011, A&A, 526, A124
Lesh, J. R. & Aizenman, M. L. 1978, ARA&A, 16, 215
Li, G., Deheuvels, S., Li, T., Ballot, J., & Lignières, F. 2023, A&A, 680, A26
Li, G., Guo, Z., Fuller, J., et al. 2020a, MNRAS, 497, 4363
Li, G., Van Reeth, T., Bedding, T. R., et al. 2020b, MNRAS, 491, 3586
Lightkurve Collaboration, Cardoso, J. V. d. M., Hedges, C., et al. 2018, Lightkurve: Kepler and TESS time series analysis in Python, Astrophysics Source Code Library
Mazumdar, A., Briquet, M., Desmet, M., & Aerts, C. 2006, A&A, 459, 589
McKinney, W. 2010, in Proceedings of the 9th Python in Science Conference, ed. S. van der Walt & J. Millman, 51
Moravveji, E. 2016, MNRAS, 455, L67
Moskalik, P. & Dziembowski, W. A. 1992, A&A, 256, L5
Moździerski, D., Pigulski, A., Kołaczkowski, Z., et al. 2019, A&A, 632, A95
Paegert, M., Stassun, K. G., Collins, K. A., et al. 2021, arXiv e-prints, arXiv:2108.04778
Pamyatnykh, A. A. 1999, Acta Astron., 49, 119
Pamyatnykh, A. A., Handler, G., & Dziembowski, W. A. 2004, MNRAS, 350, 1022
Pecaut, M. J. & Mamajek, E. E. 2013, ApJS, 208, 9
Pedersen, M. G., Chowdhury, S., Johnston, C., et al. 2019, ApJ, 872, L9
Pedersen, M. G., Escorza, A., Pápics, P. I., & Aerts, C. 2020, MNRAS, 495, 2738

Pedregosa, F., Varoquaux, G., Gramfort, A., et al. 2011, Journal of Machine Learning Research, 2825
Pigulski, A. & Pojmański, G. 2008, A&A, 477, 917
Pérez, F. & Granger, B. E. 2007, Computing in Science & Engineering, 9, 21
Raskin, G., Delabie, T., De Munter, W., et al. 2018, in Society of Photo-Optical Instrumentation Engineers (SPIE) Conference Series, Vol. 10698, Space Telescopes and Instrumentation 2018: Optical, Infrared, and Millimeter Wave, ed. M. Lystrup, H. A. MacEwen, G. G. Fazio, N. Batalha, N. Siegler, & E. C. Tong, 106985R
Reese, D., Lignières, F., & Rieutord, M. 2006, A&A, 455, 621
Rehm, R., Mombarg, J. S. G., Aerts, C., et al. 2024, A&A, in press, arXiv:2405.08864
Ricker, G. R., Winn, J. N., Vanderspek, R., et al. 2015, Journal of Astronomical Telescopes, Instruments, and Systems, 1, 014003
Saesen, S., Briquet, M., Aerts, C., Miglio, A., & Carrier, F. 2013, AJ, 146, 102
Saio, H. 1981, ApJ, 244, 299
Salmon, S. J. A. J., Eggenberger, P., Montalbán, J., et al. 2022, A&A, 659, A142
Schwarz, G. 1978, The Annals of Statistics, 6, 461
Shi, X.-d., Qian, S.-b., Zhu, L.-y., et al. 2024, ApJS, 271, 28
Shi, X.-d., Qian, S.-b., Zhu, L.-y., et al. 2023, ApJS, 265, 33
Southworth, J. & Bowman, D. M. 2022, MNRAS, 513, 3191
Stankov, A. & Handler, G. 2005, ApJS, 158, 193
Stassun, K. G., Oelkers, R. J., Paegert, M., et al. 2019, AJ, 158, 138
Sterken, C. & Jerzykiewicz, M. 1993, Space Sci. Rev., 62, 95
Struve, O. 1952, Annales d'Astrophysique, 15, 157
Takata, M. 2012, PASJ, 64, 66
Taylor, M. B. 2005, in Astronomical Society of the Pacific Conference Series, Vol. 347, Astronomical Data Analysis Software and Systems XIV, ed. P. Shopbell, M. Britton, & R. Ebert, 29
Uytterhoeven, K., Briquet, M., Aerts, C., et al. 2005, A&A, 432, 955
Uytterhoeven, K., Telting, J. H., Aerts, C., & Willems, B. 2004, A&A, 427, 593
Van Beeck, J., Bowman, D. M., Pedersen, M. G., et al. 2021, A&A, 655, A59
Virtanen, P., Gommers, R., Oliphant, T. E., et al. 2020, Nature Methods, 17, 261
Waelkens, C. 1981, A&A, 97, 274
Zhang, H. 2004, in Proceedings of the Seventeenth International Florida Artificial Intelligence Research Society Conference (FLAIRS 2004)

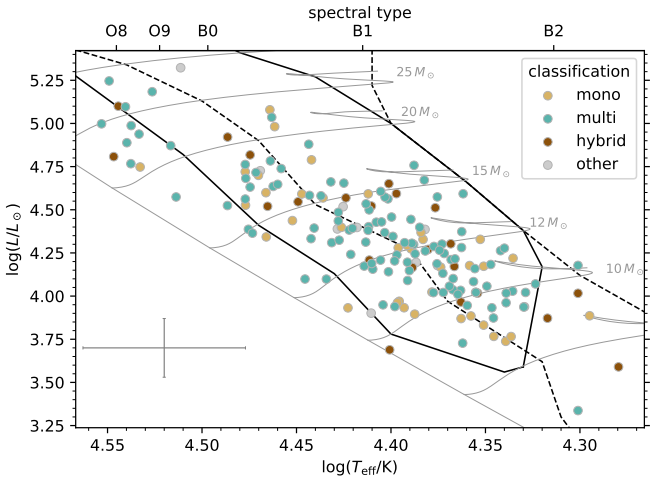

Fig. A.1. Hertzsprung-Russel diagram similar to Fig. 3 but including only the 216 stars from our *Gaia*-detected sample having TESS light curves. Each star is colour coded according to its light curve shape and content in the Fourier domain. The stars classified as *other* are discussed in the main text.

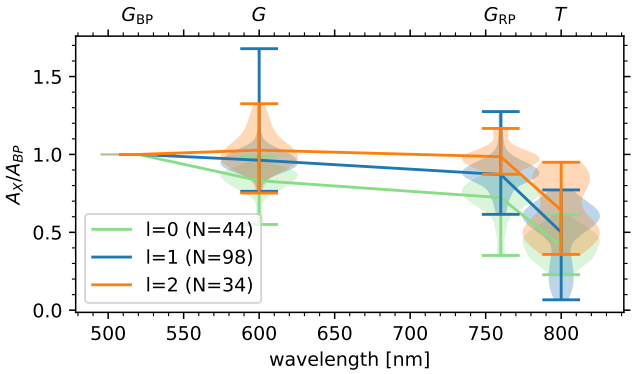

Fig. A.2. Same as Fig. 8 but based on the probabilistic assignment of mode identifications from multi-colour photometry for all modes with $p > 0.5$.

Appendix A: Additional figures

Here, we present some additional figures that are informative to the reader. Figure A.1 shows an HRD colour-coded by the light curve classification, Fig. A.2 is a repetition of Fig. 8 but this time including the mode identifications based on multi-colour photometry. Finally, we colour-code the stars in the HRD in Fig. A.3 by their mode identification.

Appendix B: Identification of the radial order

The grid modelling presented in Sect. 6.3 needs a full mode identification in terms of n, l, and m. Since our model selection is based on only the dominant mode degree, the radial order is still ambiguous and cannot be fitted in our scheme. To find the most likely radial order, we search the best fitting model for $n \in \{-2, -1, 0, 1, 2\}$ given the mode degree as determined by the multi-colour photometry.

For each star, we produced a diagnostic plot similar to Fig. B.1. It shows for all selected five radial orders the positions of all twelve considered low order radial, p, and g modes overplotted on the frequency spectrum. In these diagrams, we examined the positions of these modes with respect to all identified (and unidentified low-SNR) mode frequencies.

In the chosen example, the lowest order fit to the dominant mode ($n = -2$, orange), is able to approximately explain detected modes left to the main frequency. However, it fails to reproduce the highest detected frequency in Fig. B.1. Both the $n = -1$ (blue) and $n = 0$ (green) fit to the dominant frequency and other modes near that highest frequency. Yet, we see that the g_1-mode matches the modes near 4.5 d^{-1} better. We associate the g_1 ($l = 1$) mode with the secondary peak next to the identified frequency. The modes shown do not include any modes near 3.9 d^{-1} but higher-order g-modes might be found there for the g_1 model. In the best fitting p-mode models (purple and brown) the predicted mode frequencies do not match the observed frequencies.

In conclusion, we identified the dominant mode in this exemplary case as a g_1-mode due to the better fit of the model's mode spectrum to the overall population of visible modes in the frequency spectrum. As additional information, we obtained the χ^2 for the fitted model based on $T_{\rm eff}$, $\log L$, and f_0. In this case, the χ^2 is lowest for the g_1 model giving additional confirmation for the model preferred from visual inspection.

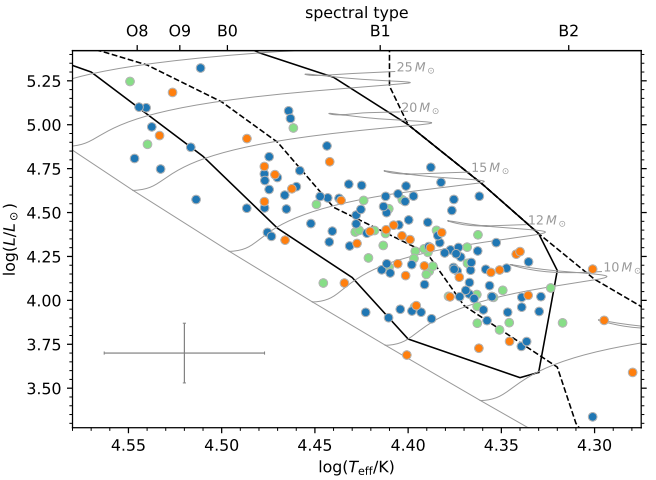

Fig. A.3. Hertzsprung-Russel diagram similar to Fig. 3 featuring only the stars with identified modes from multi-colour photometry and colour-coded by their mode degree: $l = 0$ (green), $l = 1$ (blue), $l = 2$ (orange).

Appendix C: Properties of the modelling results

C.1. Recovered values

By comparing the input and recovered values from the grid modelling, we can assess the accuracy and understand potential biases of the modelling. The three panels of Fig. C.1 show the measured and recovered $\log T_{\rm eff}$, $\log L$, and f_0. There is a slight bias towards higher effective temperatures as the majority of best fitting modes are located above the line of unity. A similar effect can be found for the luminosity, where the lower luminosity stars tend to be fitted with higher luminosity models. However, all models are within the estimated uncertainty of the measurements. The frequencies are mostly well recovered and deviate typically less than the uncertainty interval (0.5 d^{-1}) from the line of unity. We find four stars well outside of this region. These stars are among the stars with the largest differences in the luminosity and effective temperature as well. Hence, no opti-

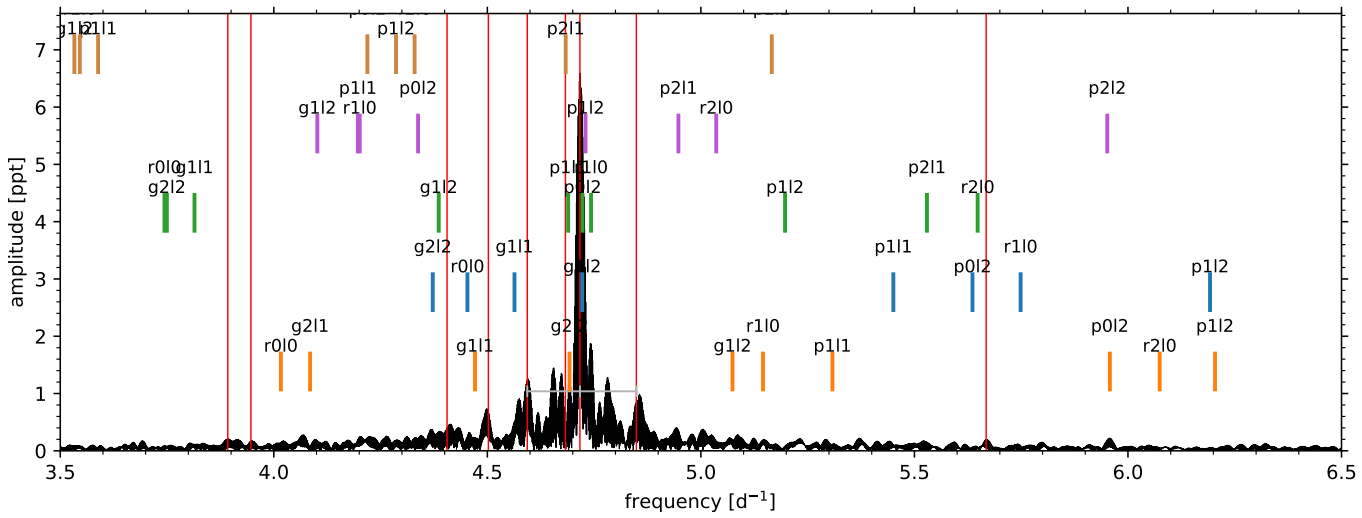

Fig. B.1. Diagnostic plot to identify the radial order n. In the background, we show in black to frequency spectrum of TIC 435101777. The lines indicate the positions of extracted independent frequencies. The short coloured lines show the positions of the modes for the best fitting model of different radial orders. From bottom to top, we show we show $n = -2, -1, 0, 1, 2$ in orange, blue, green, purple, brown, respectively. The horizontal grey line crossing the main peak, indicates the identified splitting.

mal model could be found for these stars with the adopted input physics chosen for the grid.

C.2. Ages

Due to their short lifetimes, massive stars are young in a Galactic context and can often still be found in their birth environment such as OB associations or open clusters. The *Gaia* mission has also enabled the large scale identification and description of open clusters, as well the attribution of individual stars to these groups. We use the catalogues from Cantat-Gaudin et al. (2020), Kounkel et al. (2020), and Hunt & Reffert (2023) to identify β Cep stars in open clusters and get an independent handle on their ages. We find 34 (15 %) of our sample stars to be hosted by an open cluster or co-moving group.

All the three open cluster catalogues infer the cluster ages based on their colour-magnitude diagrams and isochrones. Fig. C.2 compares our asteroseismic age to these isochronal ages. Overall our asteroseismic ages are younger than the isochronal estimates, pointing to systematic uncertainty caused by the different input physics of the isochrone and asteroseismic models in the adopted grids. However, taking into account the typical ages uncertainty of 0.2 dex for the isochronal measurements (Hunt & Reffert 2023) and 0.1 dex for the asteroseismic age, the ages are mostly in agreement.

For the two open cluster NGC 637 and NGC 5606 multiple β Cep members are in our sample. We show their members with distinct symbols in Fig. C.2. As these stars are part of coeval populations, their ages should agree within the uncertainties, unless they would be binary or multiple products. We find their asteroseismic ages exhibiting a large spread even beyond the uncertainties in the case of NGC 5606. Detailed modelling of these stars should take into account their coevality to better constrain the asteroseismic inferences and investigate if some of them could be multiples or merger products.

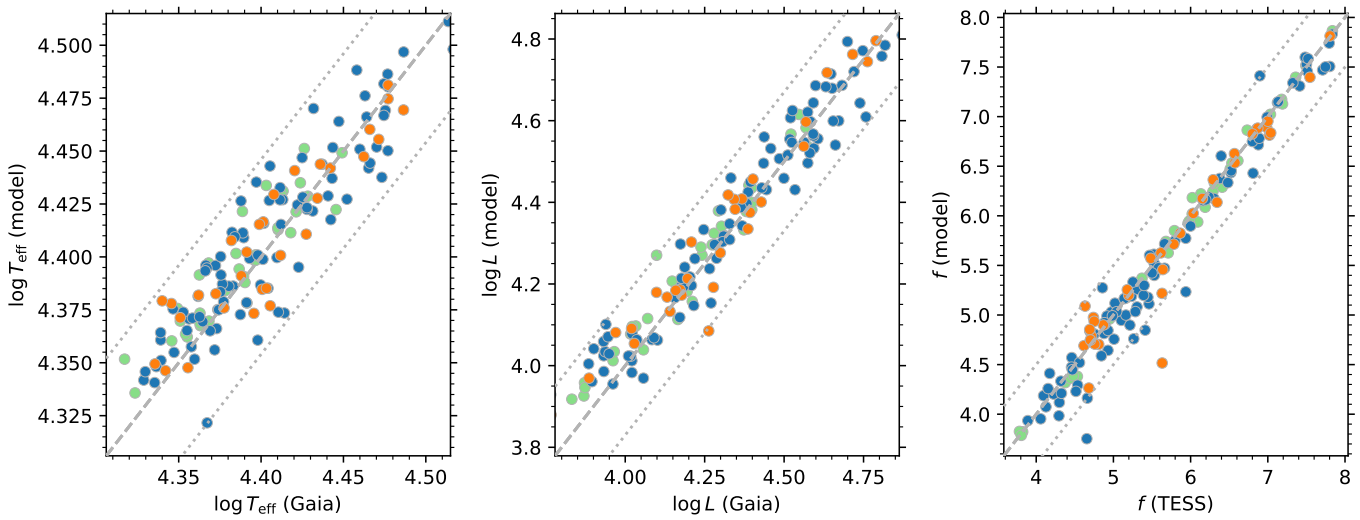

Fig. C.1. Comparison between the measured values and the properties recovered from the grid modelling. From left to right we show the effective temperature, the luminosity, and the pulsation frequency of the dominant mode. The dashed lines mark the line of unity and the dotted lines the uncertainty interval used in our fitting procedure. The colour code indicates the main pulsation mode: $l = 0$ green, $l = 1$ blue, $l = 2$ orange.

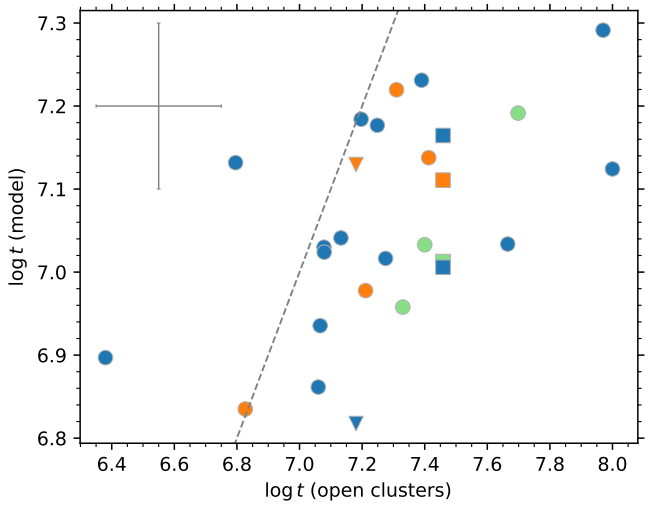

Fig. C.2. Comparison between ages for stars in open clusters and our asteroseismic ages. Members of NGC 637 are shown with square and these of NGC 5606 with triangles. The typical uncertainty is given in the upper left corner.